Acta Pharmaceutica Sinica B 2023;13(1):372–389

Chinese Pharmaceutical Association
Institute of Materia Medica, Chinese Academy of Medical Sciences

Acta Pharmaceutica Sinica B

www.elsevier.com/locate/apsb
www.sciencedirect.com

ORIGINAL ARTICLE

Highly sensitive H_2O_2-scavenging nano-bionic system for precise treatment of atherosclerosis

Xiaoyu Liang[a,†], Huiyang Li[a,†], Xuanling Li[a,c], Xinxin Tian[a], Aiai Zhang[e], Qingzhi Luo[f], Jianwei Duan[a], Youlu Chen[a], Liyun Pang[a], Chen Li[a], Xing-Jie Liang[d], Yong Zeng[b,*], Jing Yang[a,*]

[a]*Tianjin Key Laboratory of Biomaterial Research, Institute of Biomedical Engineering, Chinese Academy of Medical Science and Peking Union Medical College, Tianjin 300192, China*
[b]*Beijing Anzhen Hospital of Capital Medical University, Beijing 100029, China*
[c]*Medical College of Qinghai University, Xining 810016, China*
[d]*CAS Center for Excellence in Nanoscience, National Center for Nanoscience and Technology of China, Beijing 100190, China*
[e]*The First Affiliated Hospital of Hebei North University, Zhangjiakou 075061, China*
[f]*First Teaching Hospital of Tianjin University of Traditional Chinese Medicine, Tianjin 300381, China*

Received 8 February 2022; received in revised form 18 March 2022; accepted 22 March 2022

KEY WORDS

Highly sensitive;
H_2O_2-scavenging;
Nano-bionic system;
Atherosclerosis;
Oxidative stress;
Precise;
Target;
Pathological environment

Abstract In atherosclerosis, chronic inflammatory processes in local diseased areas may lead to the accumulation of reactive oxygen species (ROS). In this study, we devised a highly sensitive H_2O_2-scavenging nano-bionic system loaded with probucol (RPP-PU), to treat atherosclerosis more effectively. The RPP material had high sensitivity to H_2O_2, and the response sensitivity could be reduced from 40 to 10 μmol/L which was close to the lowest concentration of H_2O_2 levels of the pathological environment. RPP-PU delayed the release and prolonged the duration of PU *in vivo*. In Apolipoprotein E deficient ($ApoE^{-/-}$) mice, RPP-PU effectively eliminated pathological ROS, reduced the level of lipids and related metabolic enzymes, and significantly decreased the area of vascular plaques and fibers. Our study demonstrated that the H_2O_2-scavenging nano-bionic system could scavenge the abundant ROS in the atherosclerosis lesion, thereby reducing the oxidative stress for treating atherosclerosis and thus achieve the therapeutic goals with atherosclerosis more desirably.

*Corresponding authors.
E-mail addresses: 13501373114@163.com (Yong Zeng), yangjing37@hotmail.com (Jing Yang).
[†]These authors made equal contributions to this work.
Peer review under responsibility of Chinese Pharmaceutical Association and Institute of Materia Medica, Chinese Academy of Medical Sciences.

https://doi.org/10.1016/j.apsb.2022.04.002

1. Introduction

Atherosclerosis is a chronic inflammatory disease that is mainly caused by lipid metabolism disorders and vascular dysfunctions[1]. Lipid deposition on arterial walls promotes recruitment of macrophages and excessive oxidative cholesterol leads to the formation of extracellular lipid cores[2]. These processes aggregate reactive oxygen species (ROS) and then the oxidative state converts the low-density lipoprotein (LDL) into oxidized LDL (Ox-LDL), which in turn promotes atherosclerosis[3,4]. Animal studies have provided compelling evidence demonstrating the roles of vascular oxidative stress in atherosclerosis[5]. ROS also causes the damage to endothelial cells (EC)[6] and infiltration of macrophages. There is growing evidence on how traditional risk factors translate into oxidative stress and contribute to atherosclerosis[7]. ROS include oxygen radicals and peroxides, such as hydrogen peroxide (H_2O_2)[8] which is a central redox signaling molecule in physiological oxidative stress[9]. Clinical trials evaluating anti-oxidant supplements had failed to reduce oxidative stress in atherosclerosis[7]. Therefore, this can be a crucial issue for atherosclerosis treatment.

As one of the promising drugs for atherosclerosis, probucol (PU) is known for its hypolipidemic, anti-oxidative, and anti-inflammatory effects[10]. PU can reduce the production of lipid peroxides, delay plaque formation and inhibit the oxidative state[11]. It is considered as the first choice of antilipidemic drugs to prevent atherosclerosis. PU also inhibits the expression of inflammatory factors, improves endothelial function, thus suppressing formations of foam cells[12]. However, the bioavailability of PU is less than 10% so that it's hard to be absorbed and mostly discharged from the body[13,14]. Consequently, PU cannot produce a marked effect and its clinical applications are very limited[15].

Nanotechnology can significantly increase the bioavailability of drugs[16]. NPs enter plaque *via* the enhanced permeation and retention effect and then traverse openings between vascular EC and leak into interstitial space[17] and pass the new vessels with dysfunctional adventitia[18,19]. Then, NPs are rapidly taken up by circulating phagocytes and accumulate in atherosclerotic plaques[20]. Thus, NPs increase the therapeutic effect on atherosclerosis by enhancing passive targeting. To further improve clinical efficacy and minimize the toxicity of drugs, NPs can be modified with bio-derived membrane[21−23], such as red blood cells (RBCs)[24]. RBCs are characterized by properties of prolonging the half-life of drugs[25], improving biocompatibility[26,27], and reducing adverse reactions and immunogenicity[22,28].

Recently, nanomaterials with unique ROS-regulating properties have laid the foundation for a new generation of therapeutic approaches[29]. The elimination of H_2O_2 by materials can revert the oxidative state to the normal level of ROS and reduce the damage of oxidation. Disulfide bond, delenium bond, arylboronic esters, and peroxyoxalate bond are used to connect polymers with H_2O_2-scavenging activity[30]. Among them, the peroxyoxalate bond is more sensitive and reacts with H_2O_2 to form carbon dioxide and water which has excellent degradability and safety. The benzene ring was conjugated with peroxyoxalate to improve the sensitivity of the material to scavenge H_2O_2. It can scavenge the abundant ROS in atherosclerosis, reduce the oxidative stress, the production of lipid peroxide and the formation of plaque. Sensitive response to H_2O_2 plays a key role in the recovery of the disease.

In this study, our research team designed a new H_2O_2-scavenging polymer of polylactic glycolic acid-diphenyl ring-peroxyoxalate bond-polyethylene glycol (6s-PLGA-DAr-PO-PEG), which could reach a hypoxic microenvironment, reduce H_2O_2 level, and inhibit inflammatory responses. The H_2O_2-scavenging performance from the conjugation of diphenyl ring with peroxyoxalate bond was more sensitive than single peroxyoxalate bond. The response sensitivity can be reduced from 40 to 10 μmol/L which was close to the lowest concentration of H_2O_2 levels of the pathological environment. And the research gave the function of H_2O_2-scavenging on the degradable carrier PLGA, which made the response optimization on the simple carrier and was more conducive to the future clinical transformation. Based on 6s-PLGA-DAr-PO-PEG loaded with PU, RBC membrane was coated on the outer layer to prepare a H_2O_2-scavenging nano-bionic system (RPP-PU). RPP-PU had the best of both worlds by combining anti-oxidative stress activity and targeting effects of NPs with antioxidant and anti-inflammatory properties of PU. H_2O_2-scavenging nano-bionic system was expected to reduce oxidative state in lesions and treat atherosclerosis more effectively (Fig. 1).

2. Materials and method

2.1. Materials

DLA and GA were supplied by Jinan Daigang Bioengineering Co., Ltd. (Jinan, China). PEG (M 4000, 8074901000) and oxalyl chloride (221015) were bought from Sigma−Aldrich (St. Louis, MO, USA). 30% H_2O_2 was bought from Tianjin Guangfu Fine Chemical Research Institute (Tianjin, China). Values of analytical purity of dichloromethane (CH_2Cl_2), ethylene glycol, DMF, methanol, absolute ethanol, xylene, glacial acetic acid, hydrochloric acid, ammonia water, sucrose, acetone, chromatographic purity acetonitrile, and methanol were provided by Tianjin Jiangtian Chemical Technology Co., Ltd. (Tianjin, China). Lipopolysaccharide (LPS) (L8880), MTT (M8180), PBS (P1031, P1010), 0.25% trypsin−EDTA solution (T1300), dimethyl sulfoxide (DMSO) (D8371), 4′,6-diamidino-2-phenylindole, dihydrochloride (DAPI) solution (ready-to-use) (C0065), Tween 20 (T8220), hematoxylin-eosin (HE) Staining Kit (G1121), O.C.T. compound (4583), improved oil red O staining solution (G1261), neutral balsam (G8590) were provided by Beijing Solarbio Science & Technology Co., Ltd. (Beijing, China). Stannous octoate (S3252), potassium bromide (221864), polyvinyl alcohol (PVA, 87%−90%, wt 30,000−70,000) (P8136), DCFH-DA (D6883) and IHC Select HRP/DAB (DAB150) were bought from Sigma−Aldrich. The Micro BCA Protein Assay Kit (23235) was supplied by Thermo Fisher Scientific Inc. (Rockford, USA). DMEM High Sugar Medium (SH30243) and fetal bovine serum (FBS) (10270−106) were purchased from Gibco (Grand Island, USA). ECM medium (1001) was purchased from ScienCell (San Diego, USA). HMG-CoA ELISA Kit (YX-081325M). LCAT ELISA kit (M094732), CETP ELISA kit (M094411), APOE ELISA Kit (M094225) were purchased from Sanshu Biotechnology Co., Ltd. IL-6 Mouse ELISA Kit (KMC0061), TNF-α Mouse ELISA Kit (BMS607-3), IL-1β Mouse ELISA Kit (BMS6002), Avidin-HRP (18-4100-51) and TMB Chromogen Solution (002023) were purchased from eBioscience (Invitrogen, Carlsbad, USA).

2.2. Experimental animals

Male APOE$^{-/-}$ transgenic mice (6−8 weeks old) were purchased from SPF (Beijing) Biotechnology Co., Ltd. (Beijing, China) (Approval No.: SCXK (Jing): 2019−0010). All animal

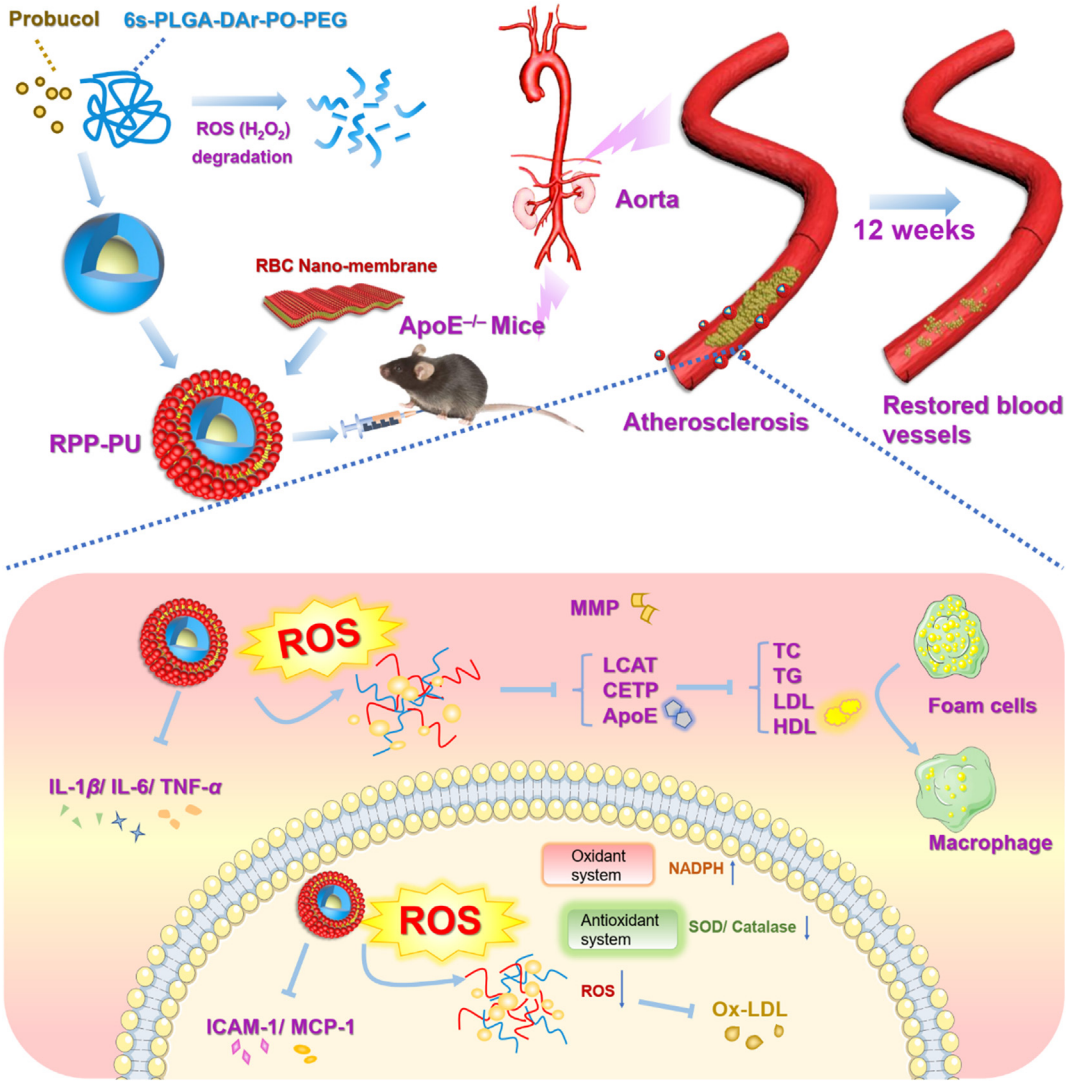

Figure 1 Preparation of RPP-PU and mechanism of improvements on atherosclerotic lesions. Nano particles (NPs) were coated with erythrocyte nanomembrane to form an H_2O_2-scavenging nano-bionic system with the ability to eliminate H_2O_2. RPP-PU can inhibit lipid and relevant enzymes and alleviate inflammatory responses.

management procedures were reviewed and ethically approved by the Center of Tianjin Animal Experiment ethics committee and authority for animal protection (Tianjin, China). (License for use of experimental animals: approval No.: SYXK (Jin):2019−0002).

2.3. Synthesis of materials-6s-PLGA-DAr-PO-PEG

2.3.1. Synthesis of 6s-PLGA

Firstly, Inositol (72.0 mg, 0.4 mmol) was used as an initiator and stannous octoate (0.004 mmol) as a catalyst. DLA (4.32 g, 30 mmol) and GA (1.16 g, 10 mmol) were monomers. 6s-PLGA was synthesized by ring-opening polymerization for 8 h at 160 °C. The synthetic procedures were similar to previous articles[31].

2.3.2. Synthesis of PEG-COOH

The end-group carboxylation of PEG was carried out by adding PEG (20 g, 5 mmol) into dioxane (300 mL). DMAP (1.524 g, 12.5 mmol) and TEA (1.262 g, 12.5 mmol) were dissolved in dioxane (50 mL). The solution was dripped into a PEG solution under the protection of nitrogen. 15 min later, succinic anhydride (SAA) (1.25 g, 12.5 mmol) was added to the solution and the reaction lasted for 24 h in the presence of nitrogen. Carboxylated PEG was obtained by repeated precipitations. The final precipitation solution was dried to constant weight in a vacuum oven. PEG-COOH was obtained after the drying process.

2.3.3. Synthesis of PEG-Ar-OH

PEG-COOH (15 g, 3.75 mmol) was dissolved in anhydrous THF (150 mL) at 30 °C. Then DCC (1.933 g, 9.375 mmol) and NHS (1.079 g, 9.375 mmol) were added in the presence of nitrogen. Tyramine (1.295 g, 9.375 mmol) was added after half an hour. Under the protection of nitrogen, the mixture underwent magnetic stirring for 24 h to allow thorough reaction and then heated to 30 °C. After repeated precipitations, the crude PEG-Ar-OH product was filtered. The crude products were dissolved in acetone to undergo the dialytic procedure for 3 days. After dialysis, the purified PEG-Ar-OH could be obtained by freeze-drying.

2.3.4. Synthesis of 6s-PLGA-Ar-OH

Firstly, hydroxybenzoic acid (0.24 g, 1.75 mmol) and DMF (0.1 mL) were dissolved in dried THF (2 mL). Oxalyl chloride (0.22 g, 1.75 mmol) was dissolved in THF (5 mL) and then dripped into the above solution in ice-bath condition under the protection of nitrogen. After 2 h, THF was removed by a rotary evaporator, and the remaining product was dissolved in THF (20 mL) again. The mixture was stirred under the protection of nitrogen, and PLGA (5 g, 0.182 mmol) and TEA (0.106 g, 1.05 mmol) were added, followed by continuous stirring overnight. When the reaction was completed, the solvent THF was removed by rotary distillation, and the product was dissolved in CH_2Cl_2 (20 mL). The crude product was then purified. The organic phase was washed by hydrochloric acid (1 mol/L, 40 mL) for three times and then it was dried with anhydrous magnesium sulfate and sodium bicarbonate. After the desiccant was removed by filtration, the organic phase was moderately concentrated and allowed to precipitate with the addition of dripped ice methanol three times. Finally, the product was dried in a vacuum dryer until a constant weight was achieved.

2.3.5. Synthesis of 6s-PLGA-DAr-PO-PEG

Oxalyl chloride can react with the hydroxyl group to form an acyl chloride group at the end[32]. First, PEG containing acyl chloride was prepared. Dry CH_2Cl_2 (10 mL) was measured and stirred with steamed oxalyl chloride (10 mmol) in an ice bath. PEG-Ar-OH (2 mmol) and TEA (2 mmol) were dissolved in dried CH_2Cl_2, poured into a dropping funnel with constant pressure, the dripping process was slow and under the protection of nitrogen, and then the mixture was stirred continuously in an ice bath for 3 h under the protection nitrogen[33]. When the reaction was completed, impurities were removed by rotary evaporation, and a solid substance was left after the drying process. Then PEG reacted with PLGA to prepare 6s-PLGA-DAr-PO-PEG. The steam-dried solid PEG containing acyl chloride (5.6 g, 1.4 mmol) was dissolved in dry CH_2Cl_2 (20 mL) and mixed evenly with TEA (0.771 mmol) in an ice bath under the protection of nitrogen. 6s-PLGA-DAr-OH (1 g, 0.036 mmol) was dissolved in dry CH_2Cl_2 (20 mL) and poured into a dropping funnel with constant pressure, then dripped into excessive PEG, and stirred under the protection of nitrogen for 48 h, followed by precipitation into the cold anhydrous ether. Finally, the mixture was dried to obtain the resulting product: 6s-PLGA-DAr-PO-PEG.

2.4. Characterization of 6s-PLGA-DAr-PO-PEG materials

FT-IR (Thermo, NICOLET is10, Waltham, USA) was used to determine the main functional groups of the synthetic material 6s-PLGA-DAr-PO-PEG, a comparison with 6s-PLGA was done. The scanning range was 400−4000 cm^{-1}.6s-PLGA-DAr-PO-PEG was dissolved in $CDCl_3$ and tetramethylsilane (TMS) was used as an internal standard. The composition of polymer materials was determined by ^1H NMR (400 MHz, $CDCl_3$ and DMSO-d_6, δ) and ^{13}C NMR (100 MHz, $CDCl_3$, δ) spectroscopy, which determined the species and quantity ratio of hydrogen and carbon atoms in polymer molecules. The glass-transition temperatures[34] within the range of 0−100 °C of 6s-PLGA and 6s-PLGA-DAr-PO-PEG were determined by Differential scanning calorimetry (DSC, TA instruments, DSC2000, New Castle, USA). Gel permeation chromatography (GPC, Waters, GPC1515, Milford, USA) was used to obtain the molecular weight.

2.5. Preparation and characterization of erythrocyte membrane NPs

The extraction process of erythrocyte membranes: fresh blood was collected and centrifuged at 3500 rpm for 10 min (Sigma, 3K15, Merck, Germany). Erythrocytes from the blood of C57BL/6 mice in the blank group were extracted. Erythrocyte membranes were obtained by hypoosmotic hemolysis, in which the extracted erythrocytes were added 0.25 × PBS and incubated on ice for 20 min, followed by squeezing and ultrasonic approach to prepare membrane-coated nano-carriers[35]. The erythrocyte membrane nano-carriers of 6s-PLGA-DAr-PO-PEG were prepared by an ultrasonic emulsification-solvent evaporation method. Taking RBC-PLGA-DAr-PO-PEG NPs loaded with PU (RPP-PU) as an example, the preparation methods were as follows: 100 mg of 6s-PLGA-DAr-PO-PEG and 30 mg of PU were precisely weighed and dissolved in CH_2Cl_2. 1% PVA solution was used as an emulsifier[36]. The material and the drug were fully mixed by ultrasound for 8 min. Erythrocytes were added into 1% PVA and mixed well. In ice-bath conditions, RPP-PU emulsion was obtained by ultrasonic emulsification for 15 min at a 25% shearing rate. The emulsion was stirred for solvent evaporation for 4 h, and then centrifuged at 10 °C, 23,000 rpm for 30 min (Beckman, Avanti J 26XPI, California, USA), and washed three times. The NPs were freeze-dried. Blank PLGA-PEG NPs (PP), RBC-PLGA-PEG NPs (RPP) were also prepared by methods described above. Finally, the NPs were sterilized by γ rays and stored at 4 °C.

2.5.1. Basic characterizations of NPs

The average particle size, distribution, and Zeta potentials of NPs were measured by a laser particle size analyzer. The morphology of NPs was observed by transmission electron microscopy (TEM, Hitachi, H−6009IV, Tokyo, Japan). The stability test was performed by dissolving the NPs in sterile water and storing the solution at 4 °C[37]. The particle size of NP was measured on Days 0, 7 and 14. Encapsulation efficiency (EE) and drug loading content (LC) of NPs were detected at 242 nm by the high performance liquid chromatography (HPLC) (Waters1525, Milford, USA). The amount of unloaded drug PU from the remaining emulsifier solution would be extracted into acetonitrile and tested by HPLC. The concentration was obtained, and then the mass of the supernatant was calculated according to the volume of the supernatant. The calculation of LC and EE were as shown in Eqs. (1) and (2):

$$\text{LC}\ (\%) = m_0/m_1 \times 100 \tag{1}$$

$$\text{EE}\ (\%) = (m - m_2)/m \times 100 \tag{2}$$

where m_0 is the mass of PU in the formulation; m_1 is the total mass of the formulation; m is the mass of PU added in the preparation; m_2 is the mass of unloaded PU.

We determined the ratio of RBCs on the surface calculated by using the surface elements. We also did the experiments to confirm the successful coating of erythrocyte membranes on NPs. SDS-PAGE gel electrophoresis was used to observe the representative membrane proteins on RBC. RBC membrane protein-TER119 was detected by BD-AccuriTM flow cytometry (BD-Accuri C6, Franklin Lake, New Jersey, USA).

2.5.2. Cytotoxicity of NPs determined by MTT assay

RAW264.7 macrophages (RAW) and EC were co-cultured with NPs *in vitro* to evaluate the cellular biocompatibility of NPs. The cell density was adjusted to 5×10^4 cells/mL. The cells were inoculated on a 96-well plate. After being cultured for 24 h, NPs (12.5, 25, 50 and 100 μg/mL) were added into the cells, followed by culture for 24 h. MTT assay was used to detect the cytotoxicity of NPs. The MTT solution (5 mg/mL) was added and the co-culture lasted for 4 h. The crystals were dissolved in DMSO. The OD value at 490 nm was measured. The calculation of cell viability was as shown in Eq. (3):

$$\text{Cell survival rate (\%)} = (\text{Absorption in the experimental group} - \text{Absorption in the blank control group}) / (\text{Absorption in the negative control group} - \text{Absorption in the blank control group}) \times 100 \quad (3)$$

2.5.3. Phagocytosis of NPs in cells

We observed the phagocytosis of NPs in cells. Fluorescent labeled coumarin-6 (Cou-6) ($M = 350$) was used to imitate PU ($M = 517.86$) because they were both liposoluble drugs with similar molecular weights. We prepared NPs loaded with free Cou-6 that is RBC-PLGA-PEG-Cou-6 NPs (RPP-Cou-6) according to the preparation process of NPs. We had co-incubated the RAW and EC in a Transwell model. We put EC on the upper layer and RAW on the lower layer. The cell concentration was diluted to 8×10^4 cells/mL. 24 h later, 100 μg/mL of Cou-6-NPs were added. Phagocytosis of NPs was observed after 2 h. The nucleus was stained with DAPI. The distribution of NPs in cells in a Transwell was observed under laser confocal microscopy (Carl ZEISS, LSM710, Oberkochen, Germany). First take photo for the upper layer of EC, and then the lower layer of RAW, and finally overlayed the two-layer photographs to obtain the merge images.

2.6. Sensitivity of NPs to H_2O_2

The morphology of NPs in PBS and that in H_2O_2 were observed by TEM. The H_2O_2 eliminating effects of NPs were tested by the Amplex red detection kit. NPs were added into 20 μmol/L H_2O_2 solution and incubated for 2 h[36]. At an excitation wavelength of 530 nm, signals were detected using a microplate reader (Thermo Varioskan Flash3001, Rockford, USA). Experimental design to define the effect of H_2O_2 on the *in-vitro* release of NPs: 24 mg NPs were suspended in 4 mL PBS, 10, 100, and 1000 μmol/L H_2O_2 PBS (pH 7.4) solution with 0.05% Tween 80 and 4 mL FBS, 10, 100, and 1000 μmol/L H_2O_2 FBS solution with 0.05% Tween 80 respectively and cultured in a shaker (150 rpm) at 37 °C[38]. The supernatant of PU solution was obtained at 2, 4, 8 h, and 1, 2, 3, 5, 7, and 14 days. The concentration of PU was determined by HPLC. The cumulative release amount was calculated.

2.7. The effects of NPs in eliminating intracellular H_2O_2

Cell-induced inflammations often lead to increased levels of ROS in cells. RAW and EC were selected to test the ability of NPs in eliminating H_2O_2. RAW and EC were cultured in a 24-well plate for 24 h, and then treated with 100 μg NPs for 2 h. Positive control was prepared by adding 1 μg LPS (about 100 nmol/L) to induce ROS production in cells[39], and the ROS level significantly increased after stimulation with LPS for 30 min. The effects on ROS in the RPP group and the control group were investigated by co-culture of cells. 10 μmol/L DCFH-DA was added to stain ROS in cells and the mixture was incubated at 37 °C for 20 min[31]. The nucleus was stained with DAPI. Fluorescence in cells was measured by flow cytometry, and fluorescence localization was measured by a confocal laser scanning microscope.

2.8. Detection of in vivo immunogenicity of NPs

Coombs' tests are divided into direct tests and indirect tests. C57BL/6J (8 weeks old, male, 20 g) mice were intraperitoneally injected with NPs 3 times a week. Blood samples were collected. Serum was obtained by centrifugation and erythrocytes were washed three times. Direct Coombs' test: 2% suspension of washed erythrocytes was added into Coombs' reagent and centrifuged for 1 min to promote agglutination. The positive result was defined by visible agglutination of erythrocytes, indicating the presence of incomplete antibodies on the surface of the erythrocyte. Indirect Coombs' test: 2% normal erythrocytes were added into serum taken from samples and directly tested. The positive result was defined by visible agglutination of erythrocytes, indicating the presence of incomplete antibodies in the tested serum. The serum levels of inflammatory factors including interleukin-1β (IL-1β), tumor necrosis factor-α (TNF-α), and interleukin-6 (IL-6) were determined by ELISA. The positive group treatment dose for LPS was 0.2 mL with all three gradients (1, 2, and 4 μg/mL). Combination of hematological parameters: hematocrit (HCT), hemoglobin volume (HGB), lymphocyte ratio (LY%), mean corpuscular hemoglobin concentration (MCHC), mean platelet volume (MPV), neutrophil count (NE) $\times 10^9$, platelet hematocrit (PCT), platelet distribution width (PDW), platelet count (PLT) $\times 10^9$, rec cell count (RBC) $\times 10^{12}$, distribution width of red blood cells (RDW), white blood cell count (WBC) was measured to observe *in vivo* compatibility of NPs.

2.9. In vivo blood concentration of NPs

C57BL/6J (8 weeks old, male, 20 g) mice were intraperitoneally injected with NPs once. Blood was collected from the lateral canthal vein at 1, 2, 4, 8, 24, 36, 48, 60, and 72 h. The drugs in blood were extracted with pure acetonitrile, and then the drug content was tested by HPLC (mobile phase: acetonitrile: water = 85:15; detection wavelength: 242 nm). Calculation of concentration was done based on the standard curve of known concentration of 1−15 μg/mL, drug-time curve was derived and changes in blood concentration were observed. The pharmacokinetics parameters of PU were calculated by DAS 2.0 software (Haibojia Pharmaceutical Technology Co., Ltd., Shanghai, China).

2.10. Construction of mouse model of atherosclerosis and administration of drugs

$APOE^{-/-}$ (8 weeks old, male, 20 g) mice were fed with a high-fat diet for 12 weeks. The mice were divided into 0.9% NaCl control, PU, RPP, and RPP-PU group. The mice were injected intraperitoneally with drugs 3 times a week at a dosage of 0.2 mL (20 mg/mL of NPs). The administration route was intraperitoneal to increase absorption area, reduce infection, reduce venous thrombosis caused by direct intravenous injection of NPs, and reduce blood toxicity[40,41]. In addition, it was more convenient for intraperitoneal administration and greatly reduced the damage to

blood vessels[42]. 12 weeks after drug administration, the animals were weighed and killed. 12 weeks later, fats around groins, kidneys, and abdominal cavity were separated, wet weight of fat was weighed and the body fat rate was calculated.

2.11. *In vivo imaging and frozen section of fluorescence distribution*

$APOE^{-/-}$ (8 weeks old, male, 20 g) mice were fed with a high-fat diet for 12 weeks. The mice were injected intraperitoneally with Cou-6, RP-Cou-6, PP-Cou-6, RPP-Cou-6 at a dosage of 0.2 mL (20 mg/mL of NPs). Then we used *in vivo* imaging (Maestro_TM, CRi, Shawano, USA) to observe and quantify the fluorescence distribution of Cou-6 in the aorta, heart, thymus, liver, spleen, lung, and kidney. At the same time, the aortic root, heart, and aorta were prepared into frozen sections and stained with DAPI and DHE. Finally, the targeting effect of NPs was observed by fluorescence microscope. Frozen sections of the aortic root were also stained by CD68 antibody to observe circulating macrophages[43].

2.12. *Magnetic resonance imaging (MRI) of atherosclerotic plaques*

MRI was employed to observe the transverse section of the abdominal aorta and the area of plaques. *In vivo*, MRI was performed by ultra-high field 7.0T MRI (BioSpec 70/20 USR, BRUKER, Germany). $ApoE^{-/-}$ mice were fed with a high-fat diet for 12 weeks and administered drugs according to dosage regimens of different groups. The mice were anesthetized with a 2.5% isoflurane/O_2 gas mixture. An average signal was used in scanning and the total imaging time of each scan was about 20 min. Each sample was scanned at baseline, MRI was performed with the same parameters as those in the baseline scanning.

2.13. *Hematological parameters*

12 weeks later, blood samples were collected. Serum levels of total cholesterol (TC), triglyceride (TG), LDL, and high-density lipoprotein (HDL) were detected by Abbott's automatic biochemical analyzer (ci4100, Abbott Laboratories, Chicago, USA). Serum levels of apolipoprotein E (APOE), 3-hydroxy-3-methyl glutaryl coenzyme A reductase (HMG-CoA), phospholipid cholesterol acyltransferase (LCAT), and cholesterol ester transfer protein (CETP) were tested by ELISA kits.

2.14. *Oil red O staining of the whole aorta and section of liver*

The whole aorta and liver were dissected and fixed. The whole aorta and sections from the liver were stained with oil red O as follows: sections were prepared from the fixed liver, treated with sedimentation with 30% sucrose and OCT embedding. Unfixed tissues were directly sliced and embedded in OCT. Frozen sections at the thickness of 6−8 μm were cut and attached to slides. The whole aorta and sections from the liver were washed with distilled water and co-cultured with oil red O working solution for 15 min, followed by differentiation with 75% alcohol and hydrochloric acid alcohol and washing with distilled water, and then the lipid droplets were stained red. The atherosclerosis plaque sizes were analyzed by Image J software (Image J 1.48, National Institutes of Health, Bethesda, USA).

2.15. *Masson staining of sections from aortic root*

Sections from the aortic root of $APOE^{-/-}$ mice were processed by Masson staining. According to the permeabilities of different tissues, anionic dyes of different molecular sizes are selected to display different tissue components. Collagen fibers, mucus, and cartilage turned blue with staining. Cytoplasm, muscle, cellulose, and colloid were stained red. Nuclei were stained purple-blue.

2.16. *HE staining of pathological sections from aortic root*

Pathological sections were prepared from the aortic root. Briefly, after deparaffinization and rehydration, longitudinal sections were stained with hematoxylin solution for 5 min, followed by staining with 1% acidic ethanol and being rinsed with distilled water. Then the sections were stained with eosin for 3 min and re-immersed in ethanol and xylene. The micro slides were examined and photographed with a microscope (Leica, DMRB, Wetzlar, Germany).

2.17. *IHC staining of pathological sections from aortic root*

Pathological sections were prepared from the aorta root, followed by IHC staining. Procedures of IHC staining included: MOMA-2 staining for macrophages, SMO staining for SMC and CD3 staining for T cells as well as CD68 staining for distributions of monocyte-macrophages and monocyte chemoattractant protein-1 (MCP-1) in mice aorta.

2.18. *Statistical analysis*

The Results of each experimental group were expressed as mean ± SD (n = 3−6). Data with normal distribution were included in the following statistical analysis of one-way ANOVA. The statistical significance of each variable was analyzed by one-way ANOVA in Graghpad Prism5 (GraphPad Software Inc., San Diego, CA, USA) ($^{*}P < 0.05$, $^{**}P < 0.01$, $^{***}P < 0.001$).

3. Results

3.1. *Characterization of 6s-PLGA-DAr-PO-PEG materials*

In our study, the synthetic process of 6s-PLGA-DAr-PO-PEG fell into two steps, as shown in the synthetic route map in Fig. 2A.

The structures of 6s-PLGA and 6s-PLGA-DAr-PO-PEG was confirmed by Fourier transform infrared, as shown in Fig. 2B. The peaks at 2998 and 2948 cm^{-1} are characteristic peaks of saturated CH bonds while the peak at 1750 cm^{-1} corresponds to C=O functional groups. After PEG modification, the absorption peak of stretching vibration of the methylene in PEG was detected at 2888 cm^{-1}. The O−H stretching peak is 3433 cm^{-1} and the absorption peak of C−O bending vibration is 1280 cm^{-1}. The absorption peaks at 1561 and 1467 cm^{-1} confirm the existence of benzene rings. The above Results show that PEG-Ar-OH is successfully combined with 6s-PLGA-Ar-OH.

DSC curves are shown in Fig. 2C. The glass-transition temperature (T_g) of 6s-PLGA was 51.01 °C, while the T_g of 6s-PLGA-DAr-PO-PEG decreased to 44.64 °C. The DSC Results varied with different materials. The main reason is that the excellent flexibility of PEG segments changed the spatial structure of block

copolymers and reduced the T_g of block copolymers. With the addition of PEG chains, the structure of PLGA copolymers becomes more complicated.

We analyzed the molecular weight change of these polymers by GPC to prove the successful modification (Fig. 2D and E). Compared with 6s-PLGA, 6s-PLGA-DAr-PO-PEG increased about six PEGs with a molecular weight of 4000 Dalton, which was consistent with the structure of synthesis design. The molecular weight change of these polymers was analyzed to prove the successful modification.

The Results of ^{1}H NMR spectroscopy in $CDCl_3$ are shown in Supporting Information Fig. S1A. Four on the far-right peaks (e–g) are magnified pictures from 6s-PLGA-DAr-PO-PEG in different drifts. CH_2 and CH were represented as 4.8 and 5.15 ppm, respectively. While the peak at 1.5 ppm corresponding to the CH_3 group in the PLGA segment, and the proportion of it was the same as that of corresponding hydrogen atoms. The typical peak at 3.6 ppm indicated the CH_2 group in PEG. There are the amplified peaks (20 times magnification) of the specific chemical shifts on the far-right side. The four amplified peaks may be as follows: 2.33 ppm (e peak) represents CH_2 group of aliphatic hydrocarbons adjacent to amide; 4.65 ppm (f peak) represents CH_2 group adjacent to amide and connected with benzene ring; 6.89 ppm (g peak) represents NH group hydrogen of the amide bond, indicating that PEG containing amide bond had been connected with PLGA; and a small peak appears at 7.58 ppm (h peak) and small double peaks at 7.1 ppm, which may be a characteristic peak on the benzene ring, indicating that the benzene ring had been successfully connected. However, due to the relatively low quantity and relatively low peak area of the benzene ring and amide bond, the hydrogen atoms in the structures of PLGA and PEG were almost invisible. These findings showed that PEG and PLGA were successfully connected.

The Results of ^{1}H NMR spectroscopy in dimethyl sulfoxide (DMSO) are shown in Fig. S1B. The peak at 2.5 ppm corresponded to DMSO solvent peak. The results are almost consistent with those of ^{1}H NMR spectroscopy in $CDCl_3$.

The Results of ^{13}C NMR spectroscopy in DMSO are shown in Fig. S1C. The far-right peaks are magnified pictures from 6s-PLGA-DAr-PO-PEG in different drifts. Peak a in 40 ppm is the CH_3 group in the PLGA segment. Peak b in 60 ppm is the CH_2 group in the PEG segment. A small peak at 67.5 ppm is the CH group in the PLGA segment and 170 ppm is the carbon atom in the carbonyl group. The far-right peaks magnified may be the carbon atom with a carbonyl group (144 ppm) and the carbon atom with a nitrogen atom (186 ppm) on amide. In the ^{13}C NMR, there are few benzene rings, amides, and peroxalate bonds. And the abundances are low. Because there are only 12 benzene rings, 6 amides, and 6 peroxalate bonds in a macromolecule. On the basis from these findings, PEG and PLGA were successfully connected.

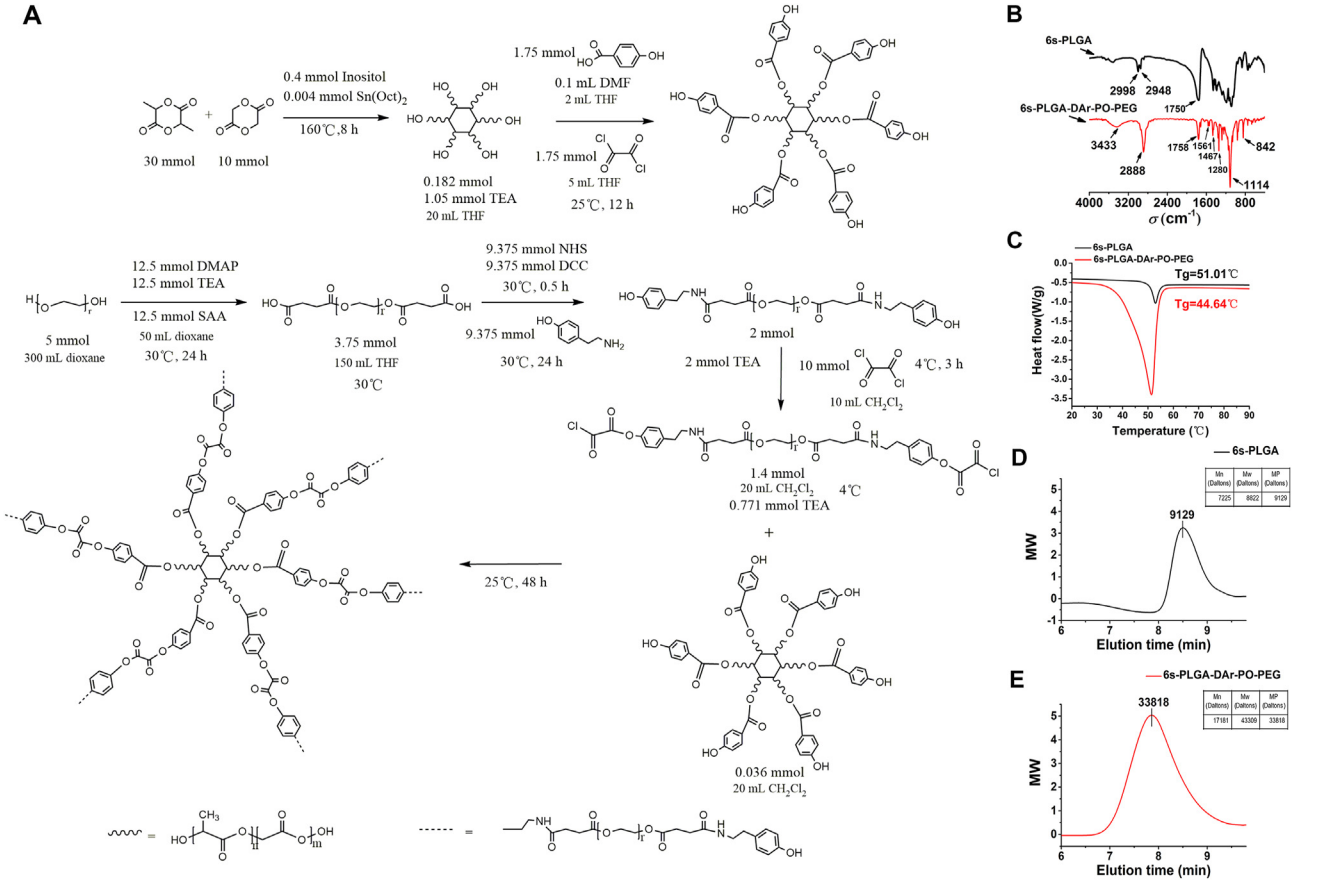

Figure 2 Synthesis and characterization of materials. (A) Synthetic route of 6s-PLGA-DAr-PO-PEG. (B) FT-IR was used to determine the main functional groups of 6s-PLGA-DAr-PO-PEG compared with 6s-PLGA. (C) The glass transition temperature of 6s-PLGA and 6s-PLGA-DAr-PO-PEG was determined by differential scanning calorimetry assay. (D, E) Molecular Results of 6s-PLGA and 6s-PLGA-DAr-PO-PEG by gel permeation chromatography.

3.2. Characterization of erythrocyte membrane-coated NPs

Pure erythrocyte membranes were extracted by ultrasound to prepare 200 nm nanoscale erythrocyte membranes. The preparation method of RPP-PU: firstly, prepared the cores of NPs with 6s-PLGA-DAr-PO-PEG as the carrier loaded with PU, and then the cores were coated with nano-scale erythrocyte membranes to form an H_2O_2-scavenging nano-bionic system (Fig. 1). NPs were administered to $APOE^{-/-}$ mice *via* intraperitoneal injections, and the improvements in atherosclerosis in the whole aorta and aortic root were observed. The mechanism of action of RPP-PU includes: RPP-PU inhibited the function of APOE, HMG-CoA, LCAT, and CETP, thus reducing the levels of TC, TG, LDL, and HDL. It reduced ROS level by materials function. And then it inhibited reverse transportation of HDL and secretions of ICAM-1 and MCP-1. H_2O_2-scavenging materials made the oxidase system decreased and the reductase system increased. And materials RPP could reduce oxidative stress. RPP-PU also restrained the production of inflammatory factors including IL-1β, TNF-α, and IL-6 (Fig. 1)[11,44–46].

3.2.1. Basic characterization of NPs

The average particle size and distribution of NPs were measured by the dynamic light scattering (DLS) method. RPP-PU was made of H_2O_2-responsive 6s-PLGA-DAr-PO-PEG containing PU. The average particle size of RPP-PU is 253.7 ± 4.76 nm and the polydispersity index (PDI) of RPP-PU is 0.078 ± 0.021 (Supporting Information Table S1). The surface charge of RPP-PU is −10.44 ± 0.84 mV.

The morphology and particle size of RP-PU, PP-PU, and RPP-PU were observed by TEM (Fig. 3A–C). The NPs present uniform sizes without adhesion. The NPs are spherical, with particle size at about 200 nm. The double-layer membrane structure of RP-PU and RPP-PU could be observed after modification with the coating of erythrocyte membranes. The outer layer consists of semi-translucent membranes and the inner layer consisted of NPs with a solid core–shell structure. PP-PU shows monolayer NPs without the coating of erythrocyte membranes.

We also measured the stability of NPs in FBS. No significant changes were observed in the particle size, distribution, and Zeta potential of RP-PU, PP-PU, RPP-PU within 14 d (Fig. 3D–F). The particle sizes of RP-PU, PP-PU, RPP-PU are about 200 nm or so. The PDI of RPP-PU was the smallest within 14 days and the zeta potential was the lowest, which shows that its stability is the best. The Results indicate that these NPs presented strong stability. As shown in Table S1, the Encapsulation Efficiency of RPP-PU reached up to about 97%. The Loading Capacity of RPP-PU was about 29%. We found that the LC of the drug was increased with modification of erythrocyte membranes, possibly due to the lipophilicity of drugs.

The ratio of RBCs on the surface calculated as shown in Supporting Information Table S2. Iron is an important component of erythrocyte hemoglobin. To some extent, we get the content of the erythrocyte membrane indirectly from the content of iron. The content of the iron atom was 0.34% in NPs. In routine blood tests, we learned that a liter of male blood contains about 11.6–31.3 μmol iron and 3.5×10^{12}–5.5×10^{12} red blood cells. After calculation, 100 mg NPs contain 340 μg (6.07 μmol) iron that can package about 0.68×10^{12}–2.87×10^{12} red blood cells. The type of membrane proteins had no changes after coating on NPs in comparison to the erythrocyte membrane. In literature, the erythrocyte membrane made of ultrasonic method had verified that the membrane protein does not change after wrapping by SDS-PAGE gel electrophoresis[47,48]. The Results show that RP and RPP contained RBC membrane proteins (Supporting Information Fig. S2). The coating of the erythrocyte membrane on this system had been identified.

3.2.2. Detection of cytotoxicity of NPs

The cell viability of EC and RAW were more than 90% respectively with stimulating by all groups (Fig. 3G and H). There was no significant difference in cell survival rate among these groups at different concentrations. The Results indicate that RP, PP, RPP, and RBC all had good biocompatibility. The results also prove that this material presented no significant cytotoxicity. Based on the appropriate particle size, outstanding stability, excellent drug loading capacity, and drug-releasing capacity, biocompatible RPP-PU was expected to be used in drug delivery systems.

3.2.3. Cellular uptake of NPs

The green fluorescence of Cou-6 was observed in RPP-Cou-6-treated RAW and EC. We observed the phagocytosis of the upper and lower layers respectively, and also merged the two layers of cells to observe together. The phagocytosis of all NPs was stronger than that of the free Cou-6 group (Fig. 3I). The NPs released strong fluorescence signals, indicating a reliable ability of NPs in intracellular internalization. Compared with the NPs in each group, PP-Cou-6 and RPP-Cou-6 were more selective engulfed in macrophage and less in EC and RPP-Cou-6 showed a more significant statistical difference compared with RP-Cou-6 in EC (Fig. 3J and K). The phagocytosis of RP-Cou-6 was consistent in EC and RAW. This indicates that RP-Cou-6 was not selective in EC and RAW. We repeated the phagocytosis experiment and compared the two groups (RP and RPP) together to observe more intuitively (Supporting Information Fig. S3). There is significant difference in fluorescence intensity inside RAW between RP group and RPP group. It demonstrates that the higher selectivity of RPP NPs for RAW. Group of EC incubated without LPS had been added. The Results show that few RPP-PU could be taken up by normal EC.

3.3. Test of NPs' sensitivity to H_2O_2

The morphology of RP-PU, PP-PU, RPP-PU was observed by TEM (Fig. 4A–C). PP-PU and RPP-PU are spherical and present good dispersibility in the absence of H_2O_2. In the presence of H_2O_2, the morphology of RPP became irregular and the aggregation of NPs caused by the breakage of the peroxalate bond in H_2O_2. It indicates that PP-PU and RPP-PU had H_2O_2 responsiveness. And RP-PU did not change in the absence or presence of H_2O_2.

The cumulative drug release curve of RPP-PU in PBS is shown in Fig. 4D. More than 15% of PU released on the first day, followed by a slow and sustained release in phosphate-buffered saline (PBS) buffer (PH 7.4, 0.01 mol/L) for 14 days. RPP released faster in H_2O_2 than PBS, as shown in Fig. 4D, indicating responsiveness of RPP to H_2O_2. As H_2O_2 concentration increased, the release would be accelerated. We also did the drug release studies in FBS in the simulated *in vivo* environment (Fig. 4E). The release trends of NPs in PBS and FBS are consistent. NPs released more in the increase of H_2O_2 concentration. However, NPs released faster in FBS than in PBS (Fig. 4D and E). FBS contained lipids, and probucol was a lipophilic drug. So, NPs released faster in FBS. The release of different NPs (RP-PU, PP-PU, RPP-PU) in

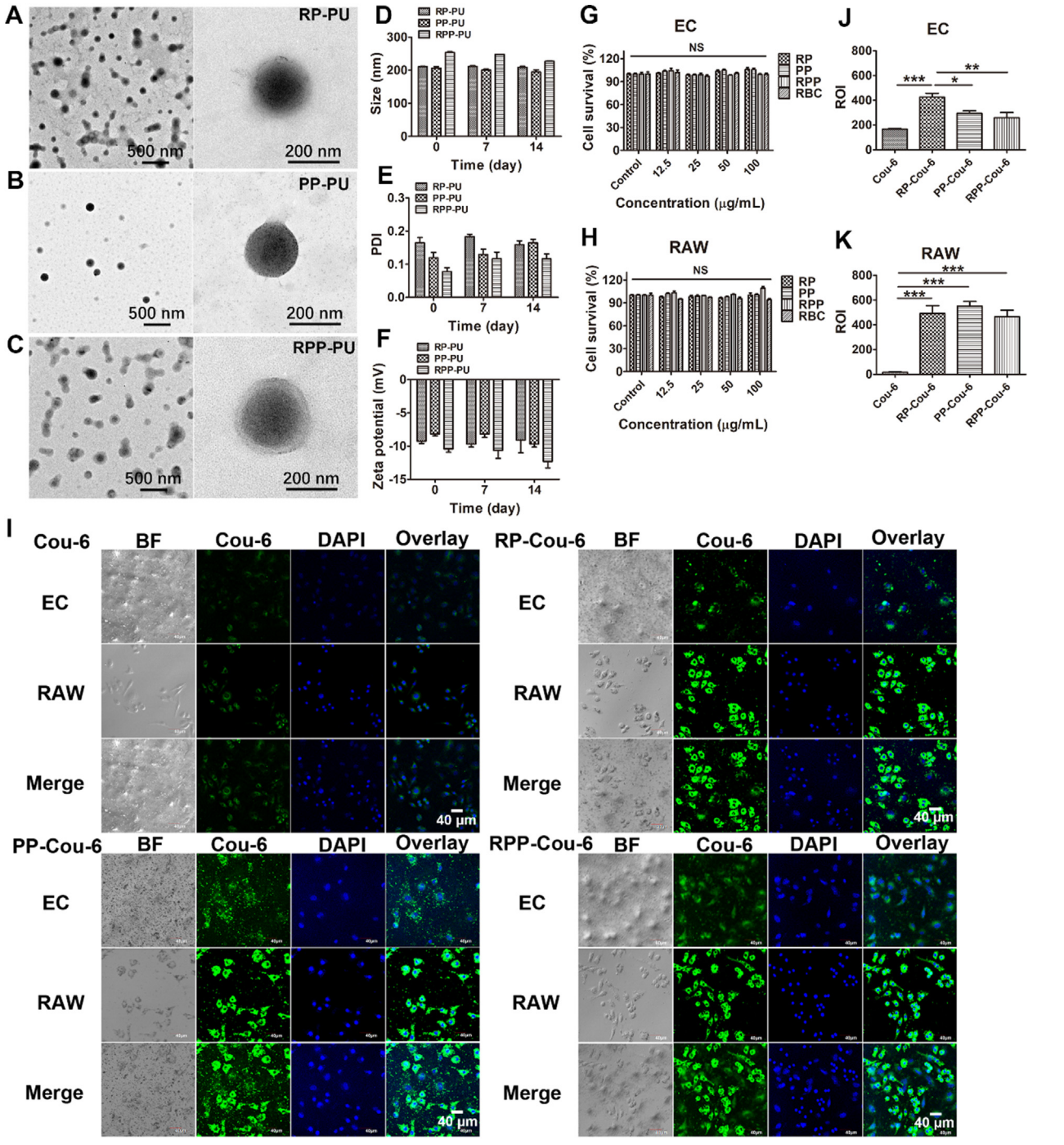

Figure 3 Characterization of erythrocyte membrane NPs. (A–C) The morphology and particle size of RP-PU, PP-PU, RPP-PU were observed by TEM. (D) The average particle size in 14 days. The stability of particle size of NPs was observed. (E) The polydispersity index of size in 14 days. (F) Zeta potentials of NPs in 14 days. (G, H) Cell viability assays of EC and RAW were done by MTT. (I) Phagocytosis of fluorescent Cou-6, RP-Cou-6, PP-Cou-6, and RPP-Cou-6 in RAW and EC in transwell. Scale bars = 40 μm. (J, K) Quantitative statistical analysis of fluorescence data was done to describe the uptakes of NPs in RAW and EC. Data are presented as mean ± SD ($n = 5$). *$P < 0.05$, **$P < 0.01$, ***$P < 0.001$. NS, not significant.

different H_2O_2 concentrations was observed (Fig. 4F–I). When PP were modified by RBCs, the leakage and release of the drug reduced by the action of RBCs coated on the outer layer, and the release of RPP slowed down. When the concentration of H_2O_2 increased, the release behavior of PP-PU was similar to RPP-PU. RPP-PU was more sensitive to low concentrations of H_2O_2, while it was similar to PP-PU in high concentrations. Mathematical modeling was calculated the release kinetics by Origin 2016. The peroxide effect on the release kinetics was that the RBC membrane reacted with H_2O_2 first, and then the H_2O_2 responsive material 6s-PLGA-DAr-PO-PEG reacted with H_2O_2. The rupture of the material accelerated the release. Most of the drug sustained-

release followed the first-order or Higuchi kinetic process. We fitted the curve and the first-order or Higuchi kinetic equation are listed in the supporting document shown in Supporting Information Table S3. We also did the responsive release in H_2O_2 solution ranged from 0 to 50 μmol/L (Supporting Information Fig. S4). We found that the RPP nanoparticles still had sensitive response under the condition of low concentration of H_2O_2. And the release was accelerated under the condition of H_2O_2, which had statistical significance from other groups. The experiments provided clear evidence on the H_2O_2 sensitive drug release *in vivo*. The release of RPP nanoparticles in the *in vivo* environment stimulated by LPS is significantly faster than that in the environment without LPS (Supporting Information Fig. S5).

NPs (1 mg/mL) were suspended in H_2O_2 solution and incubated for 2 h. P is blank NPs of 6s-PLGA; PP is blank NPs of 6s-PLGA-DAr-PO-PEG; RPP is blank NPs of RBC-6s-PLGA-DAr-PO-PEG. As shown in Fig. 4J, there is no statistical difference between control, PEG, and P, so that they had no response to H_2O_2. In comparison with PP and PEG solutions, RPP (1 mg/mL) solution exhibited a more significant H_2O_2-eliminating capacity. In the context of rapid disintegration of RPP, the elimination rate of H_2O_2 could reach up to more than 90% in the first 2 h. Therefore, we validated the responsiveness of RPP to H_2O_2. H_2O_2 in the PEG solution was not eliminated. And the higher the material concentration, the stronger the scavenging effect on H_2O_2 (Fig. 4K). The H_2O_2-scavenging material 6s-PLGA-DAr-PO-PEG contains the diphenyl ring linked peroxyoxalate bond; 6s-PLGA-PO-PEG does not contain diphenyl ring but contains peroxyoxalate bond. 6s-PLGA-DAr-PO-PEG removed almost 10% H_2O_2 more than 6s-PLGA-PO-PEG at the same concentration (Fig. 4L). The Results show the conjugated peroxyoxalate bond of diphenyl ring could remove H_2O_2 better with a highly sensitive scavenging efficiency.

The hydrolysis of materials in the same conditions was observed. The molecular weight of 6s-PLGA and 6s-PLGA-DAr-PO-PEG were detected in 10 μmol/L H_2O_2 (Supporting Information Fig. S6). The Results indicate that the molecular weight of 6s-PLGA was almost unchanged in the presence or absence of H_2O_2, and there is no statistical difference. However, the molecular weight of 6s-PLGA-DAr-PO-PEG was decreased in

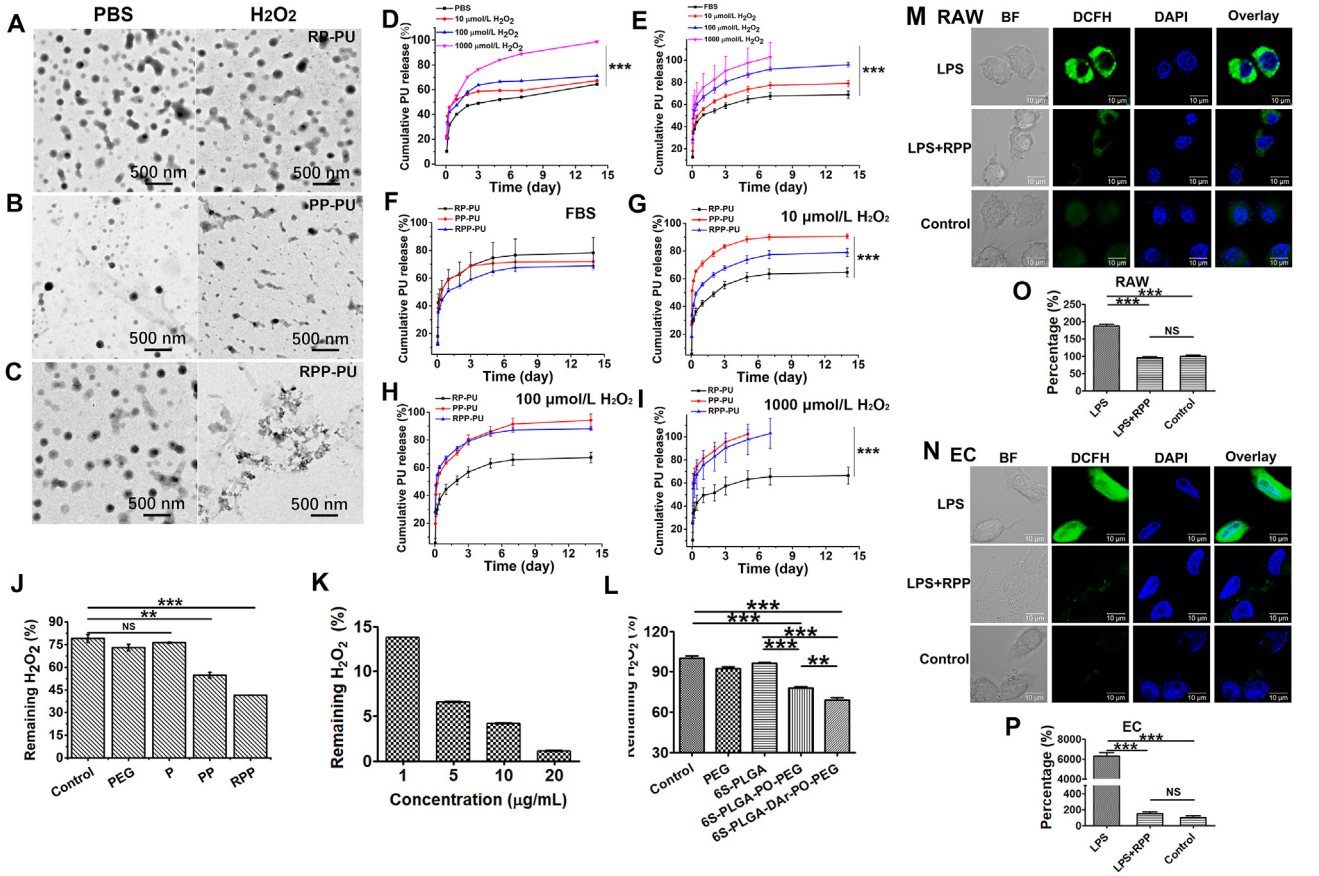

Figure 4 Elimination of H_2O_2 by NPs. (A–C) The image and morphology of NPs (RP-PU, PP-PU, RPP-PU) in PBS or H_2O_2 were observed by TEM. (D) *In vitro* release of RPP-PU was observed in PBS or H_2O_2 solution with a concentration of 10, 100, and 1000 μmol/L in PBS. (E) *In vitro* release of RPP-PU was observed in FBS or H_2O_2 solution with a concentration of 10, 100, and 1000 μmol/L in FBS. (F–I) *In vitro* release of RP-PU, PP-PU, and RPP-PU was observed in FBS or H_2O_2 solution with a concentration of 10, 100, and 1000 μmol/L in FBS. (J) Determination of residual H_2O_2 at 2 h after NPs incubation. (K) Removal of H_2O_2 by RPP with different concentrations. (L) Removal of H_2O_2 by different materials. (M–P) The ability of NPs to eliminate H_2O_2 in RAW and EC. 1 μg LPS (about 100 nmol/L) induced ROS production in all groups except the negative control group. Images of NPs in eliminating H_2O_2 in RAW (M) and EC (N) and corresponding quantitative Results (O, P). Scale bars = 10 μm. Data are presented as mean ± SD ($n = 5$). $^{**}P < 0.01$, $^{***}P < 0.001$. NS, not significant.

the presence or absence of H_2O_2. The results indicate that 6s-PLGA-DAr-PO-PEG degraded in H_2O_2 and proved the H_2O_2 response of the material from another side.

We also found that RBC has the function of scavenging H_2O_2 (Supporting Information Fig. S7), which is a new discovery different from other research on cell membrane coating. RBC membrane and H_2O_2 responsive materials can work together to resist atherosclerotic oxidative pathological microenvironment. And in the H_2O_2-scavenging experiment, we verified that the scavenging effect of RPP was far more than that of PP group, so the synergistic effect of RBC and PP was significantly displayed in RPP group, so we used RPP-PU group with more significant synergistic effect *in vivo*.

3.4. *Elimination of ROS by NPs in cells*

The Results show that the ROS level in RAW cultured by RPP was significantly lower than that in the control group (Fig. 4M and O). We found similar results that the ROS level in EC was also eliminated a lot by RPP (Fig. 4N and P). The level of ROS after RPP clearance was not statistically different from the control group. It means RPP could reduce ROS in LPS- stimulated RAW and EC, and could reduce to normal ROS levels. RPP could clear ROS well both in cells and *in vitro*, which laid a good foundation for removing ROS in animals.

3.5. *In vivo blood drug concentration of NPs*

The *in vivo* blood drug concentration of NPs shows that RP-PU and RPP-PU have the same peak time, which might be due to red blood cells' increasing cycle time. PP was not wrapped by red blood cells, so the peak time is relatively early (Fig. 5A). About the free PU group and RPP-PU plasma concentration: the C_{max} values are 27.026 ± 12.487 and 28.212 ± 3.217 μg/mL, respectively, reaching peak times of 0.5 and 24 h, respectively. The areas under the curve (AUC_{0-t}) are 639.221 ± 11.392 and 905.343 ± 54.080 μg h/mL, respectively. Compared with PU, RPP-PU had the advantages of C_{max} and AUC_{0-t} values are 1.04 and 1.42 times of PU group respectively. NPs prolonged the peak time of the drug. The Results show that RPP-PU could significantly improve the effects of drug absorption and bioavailability. Delay in the peak of drug concentration proved that RPP-PU effectively protected the drug and facilitated the action of a large amount of the drugs, thus ensuring more favorable therapeutic effects delivered by RPP-PU in the treatment of atherosclerosis.

$ApoE^{-/-}$ mice species are derived from wild-type C57BL/6J mice and the experimental dosage was huge, we selected the wild-type C57BL/6J mice with the closest genotype and economic utility to verify the pharmacokinetic study *in vivo*. Plaque-bearing $ApoE^{-/-}$ mice would be the best choice, and we would choose $ApoE^{-/-}$ mice for the pharmacokinetic study when we did the next study.

3.6. *In vivo immunogenicity of NPs*

The erythrocytes from all groups (control, RP, PP, RPP) in the test tube were shown after centrifugation and suspension from direct Coombs' test (Di) and indirect Coombs' test (Indi). The macro images are shown in Fig. 5B. After centrifugation and then suspension, no erythrocyte aggregation was observed. The micro images (10 ×) are shown in Fig. 5C from Di and Indi. There was also no hemagglutination of erythrocytes. Results from Coombs' direct test reveal no hemagglutination of erythrocytes in all groups under both visual and microscopic observations. Therefore, no anti-erythrocyte antibodies were produced, suggesting a more reliable safety of this preparation. The results from indirect tests are consistent with those from direct tests and confirm the biosafety and non-immunogenicity of all NPs (Fig. 5B and C).

The levels of inflammatory cytokines including IL-1β, IL-6, and TNF-α in serum were very low. The Results confirm that NPs did not cause inflammation. Compared with the positive control group with LPS stimulation, productions of inflammatory factors including IL-1β, IL-6 and TNF-α were very low after treatment with NPs, reflecting the favorable biocompatibility and the non-proinflammatory property of NPs (Fig. 5D–F).

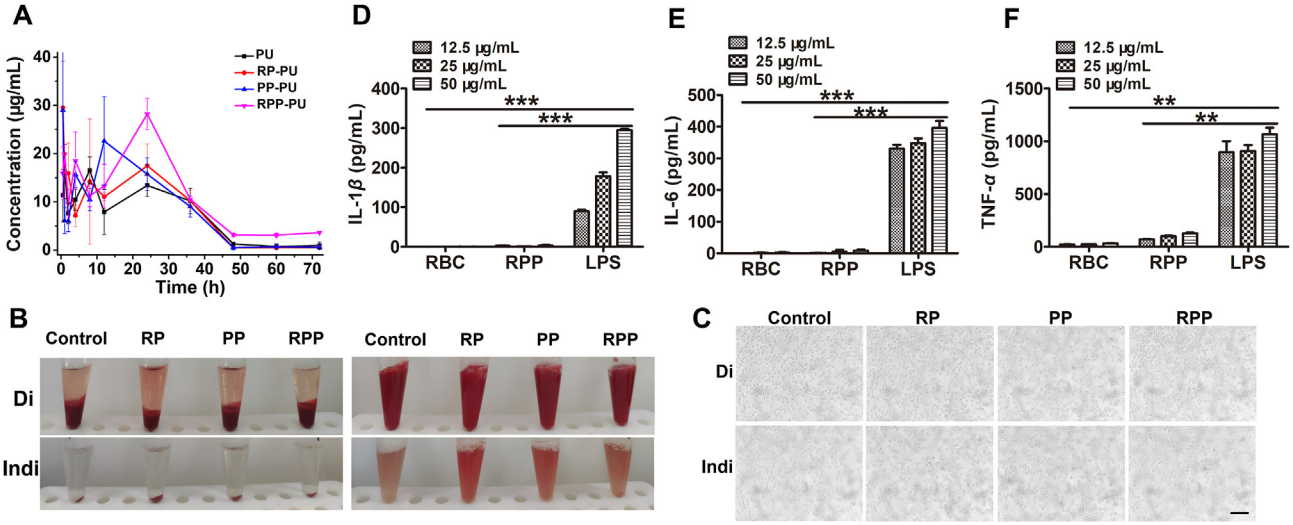

Figure 5 *In vivo* blood drug concentration and safety of NPs. (A) *In vivo* blood drug concentration at 1, 2, 4, 8, 24, 36, 48, 60 and 72 h, and the drug was extracted. Blood drug concentrations were measured. (B) The macro images of RBC in a test tube after centrifugation (left) and suspension (right) from the direct Coombs' test (Di) and indirect Coombs' test (Indi). (C) The micro images of RBC from the Di and Indi. Scale bars = 200 μm. (D–F) Effects of NPs on inflammatory factors including IL-1β, IL-6, and TNF-α. Data are presented as mean ± SD (n = 4). $^{**}P < 0.01$, $^{***}P < 0.001$ *vs* LPS group. NS, not significant.

We also tested the combination of hematological parameters of RBC and RPP (Supporting Information Fig. S8) and found no significant difference between them and the control group in HCT, HGB, LY%, MCHC, MPV, NE $\times$ 10^9, PCT, PDW, PLT $\times$ 10^9, RBC $\times$ 10^{12}, RDW, and WBC. The above Results show that both RBC and RPP had no immunogenicity.

3.7. *In vivo imaging and frozen section verification of NPs targeting AS*

The Results show that the strongest whole aorta fluorescence was RPP-Cou-6, followed by PP-Cou-6, followed by RP-Cou-6, and the weakest was Cou-6 (Fig. 6A and B). Only RPP-Cou-6 and free Cou-6 had a significant difference in cardiac fluorescence, but no difference in other groups. In organs, NPs were mainly distributed in the liver and less in other organs. In the liver, the fluorescence of RPP-Cou-6 was the strongest, followed by RP-Cou-6 and then PP-Cou-6, and the weakest was Cou-6 (Fig. 6C and D). PP/RPP was more distributed in blood vessels than RP. It indicates that H_2O_2-scavenging material can target blood vessels. RP/RPP was more distributed in the liver than PP. It may be because red blood cells have long circulation and can stay in tissues for a long time. RPP combined the good targeting effect of PP and the tissue retention effect of RP. We also observed fluorescence distribution in organs at different time points of Cou-6 and RPP-Cou-6 (Supporting Information Fig. S9). We found that RPP-Cou-6 was always stronger than Cou-6 at these time points. At the same time, we found that Cou-6 had almost no fluorescence in blood vessels at 24 h, while the fluorescence of RPP-Cou-6 was still very strong. It suggested that RPP-Cou-6 had a good long circulation effect and targeting effects in blood vessels.

The frozen sections of the aortic root show that there is no significant difference between RP and the control group, and the fluorescence of PP-Cou-6 and RPP-Cou-6 is significantly different from the RP group. It also shows the aortic targeting of PP-Cou-6 and RPP-Cou-6 (Fig. 6E and F).

We also observed ROS by DHE staining on the aortic root and found that PP and RPP could significantly reduce ROS at the lesion site, while RP hardly reduced ROS (Fig. 6E and G). DHE staining on the heart and aorta shows similar Results (Supporting Information Fig. S10). The results show that RPP could precisely target the aorta and reduce ROS at the lesion site. PP-Cou-6 nanoparticles and RPP-Cou-6 nanoparticles had the similar accumulation in atherosclerotic lesions, while the ROS level of RPP-Cou-6 nanoparticles was lower than that of the other. The results are same as the *in-vitro* results of elimination of H_2O_2 by NPs. RPP could reduce ROS more than PP. There were a lot of proteins on the surface of RBC membrane. Disulfide bonds of RBC membrane proteins could react with H_2O_2[30]. Therefore, the core of PP in RPP played a role in targeting the high ROS site of the lesion, while RBC could assist in reducing ROS. Therefore, RPP had the same targeting effect as PP, but the effect of removing ROS was stronger.

We observed the nanoparticles and circulating macrophages in the aortic root (Supporting Information Fig. S11). The Results show that a large number of RPP nanoparticles gathered at the lesion site, and CD68 stained circulating macrophages were also very abundant. The Cou-6 and CD68 double positive cells of aorta were quantified by flow cytometry. The double positive cells in RPP group were the most, showing that RPP nanoparticles were easier to be phagocytized by circulating macrophages and delivered to the lesion site.

3.8. *MRI findings from plaques in abdominal aorta*

The red circle in the middle defined the transverse section of the abdominal aorta. The black part indicated the excellent permeability of blood vessels and the white part represented blocked signals from plaques of adipose tissues. The quantify process was as followed: Firstly, the white area we located was the blood vessel in the red circle, that is, the lipid content of the blood vessel section was calculated to quantify aorta lipid. Lipids outside the vessel cross-section were not counted. Secondly, lipid SUM came from lipids (white part in the figure) in typical Sections 1 and 2, that is, adipose tissues in the liver and near the kidney area. Finally, the images showed only one layer of the sweeping image, and we calculated the average white area of at least four layers.

Results from the control group were almost all white, suggesting a very large area of adipose plaques. There were a few white plaques found in RPP and PU groups, indicating certain therapeutic effects. In the RPP-PU group, abdominal aortic plaques were largely removed and the blood vessels were transparent, deposit of visceral fat was observed to be reduced (Fig. 6H–K). PU group had a whiter area which was outside the vessel cross-section. These lipids are not in the aorta but the surrounding tissues. In comparison with findings from other groups, adipose tissues in the liver and near the kidney area only in the RPP-PU group were significantly reduced. The results showed that RPP-PU had a strong lipid-scavenging effect.

3.9. *Oil red O staining of the whole aorta*

The Results from oil red O staining showed that the adipose plaques were stained red. The red part was the plaque area. The proportion of plaque was obtained by comparing the plaque area with the total vascular area. Results from the quantitative analysis show that in comparison with the control group and free PU group, the area of adipose plaques in the RPP-PU group was lower, presenting significant differences. RPP-PU significantly reduced the area of plaques (Fig. 7A and B). However, free PU and RPP did not have a significant difference from the control group.

We also made the oil red O Staining of cross-section from the liver (Supporting Information Fig. S12). The Results show that the RPP-PU group significantly reduced the lipid of the liver, which was significantly different from other groups. Although there was no statistical difference between the RPP group and control group, it could be observed that the RPP group had the trend of reducing lipids, because the material reduced oxidized lipoproteins, and the lipid-scavenging function of cells itself was improved. PU can reduce lipids, but there was no significant decrease compared with RPP-PU. This experiment proved that RPP-PU had a powerful function of scavenging lipids.

The Results show that the body fat rates of mice in the RPP-PU group were significantly lower than those in the control and PU groups (Fig. 7C), indicating the superior lipid-lowering effects with treatments of NPs. And the ROS levels in the aorta of mice in both the RPP group and RPP-PU group were significantly reduced, indicating the impressive strength of RPP and RPP-PU in eliminating ROS (Fig. 7F), thus reducing damages caused by oxidative stress. RPP-PU had an obvious lipid-lowering function.

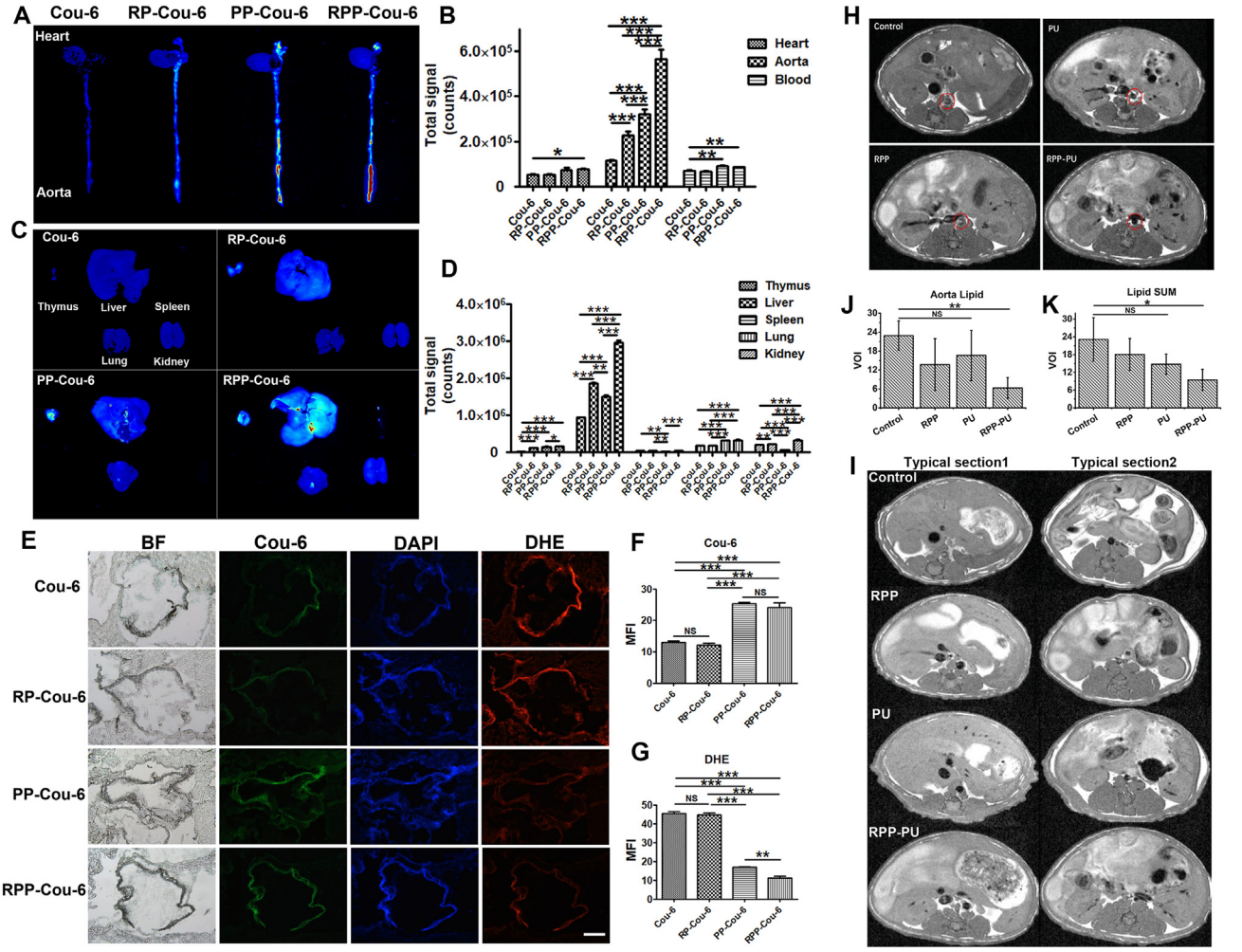

Figure 6 NPs targeting atherosclerosis and MRI cross-sections in mice. (A) Fluorescence distribution in heart and aorta. (B) The quantity of fluorescence total signal in the heart, aorta, and blood. (C) Fluorescence distribution in thymus, liver, spleen, lung, and kidney. (D)The quantity of fluorescence total signal in organs. (E) Frozen sections of the aortic root. DHE stained for ROS. Scale bars = 200 μm. (F, G) The quantity of Cou-6 and DHE in the aortic root. (H) Typical images of MRI of the abdominal aorta from different groups. The red circle in the middle outlined the cross-section of the abdominal aorta. The black parts suggested blood vessels with excellent transparency, the white parts indicated blocked signals from plaques of fat. (I) Visceral fat in the liver (typical Section 1) and fat near the kidney (typical Section 2). (J) Quantity of plaques in the abdominal aorta. (K) The amount of visceral fat in the liver and the amount of fat near the kidney. Data are presented as mean ± SD ($n = 4$). $^*P < 0.05$, $^{**}P < 0.01$, $^{***}P < 0.001$. NS, not significant.

PU itself had antioxidant properties, so ROS was reduced. In addition, RPP and RPP-PU reduced ROS significantly compared with the control group. The benefits of RPP and RPP-PU were promoting lipid metabolism rather than causing hyper oxidation of lipids. So, the NPs reduced oxidative state, reduced oxidized lipoproteins, resolved endothelial dysfunction, and provided a desirable environment to inhibit the formation of fibrosis.

3.10. Masson staining of aortic root sections

Masson staining is mainly used in differential staining of collagen fibers and muscle fibers. Compared with the control group, RPP-PU could significantly reduce the amount of collagen and fibers. The content of collagen in the RPP-PU group was also lower than that in the free PU group (Fig. 7D and E). Therefore, RPP-PU can reduce tissue fibrosis and protect myocardial function. Similar Results were obtained from sections taken from the transverse section of the infarct sites (Supporting Information Fig. S13). The results show that RPP did not cause vascular fibrosis, and contributed to the recovery of blood vessels and reduced fibrosis.

3.11. Hematological parameters

Twelve weeks later, blood serum was separated and frozen. The Results suggest that administration of RPP-PU significantly reduced the levels of TC, TG, and LDL. And RPP-PU had a trend to reduce the levels of HDL. In comparison with PU, RPP-PU reduced the serum lipid levels more effectively (Fig. 7G). RPP-PU also significantly decreased the enzymatic activities of HMG-CoA, LCAT, CETP, and APOE, demonstrating its effects on metabolizing lipids (Fig. 7H). Compared with the PU group, the levels of inflammatory factors in the RPP-PU group were inhibited, implying the favorable therapeutic effects delivered by RPP-PU.

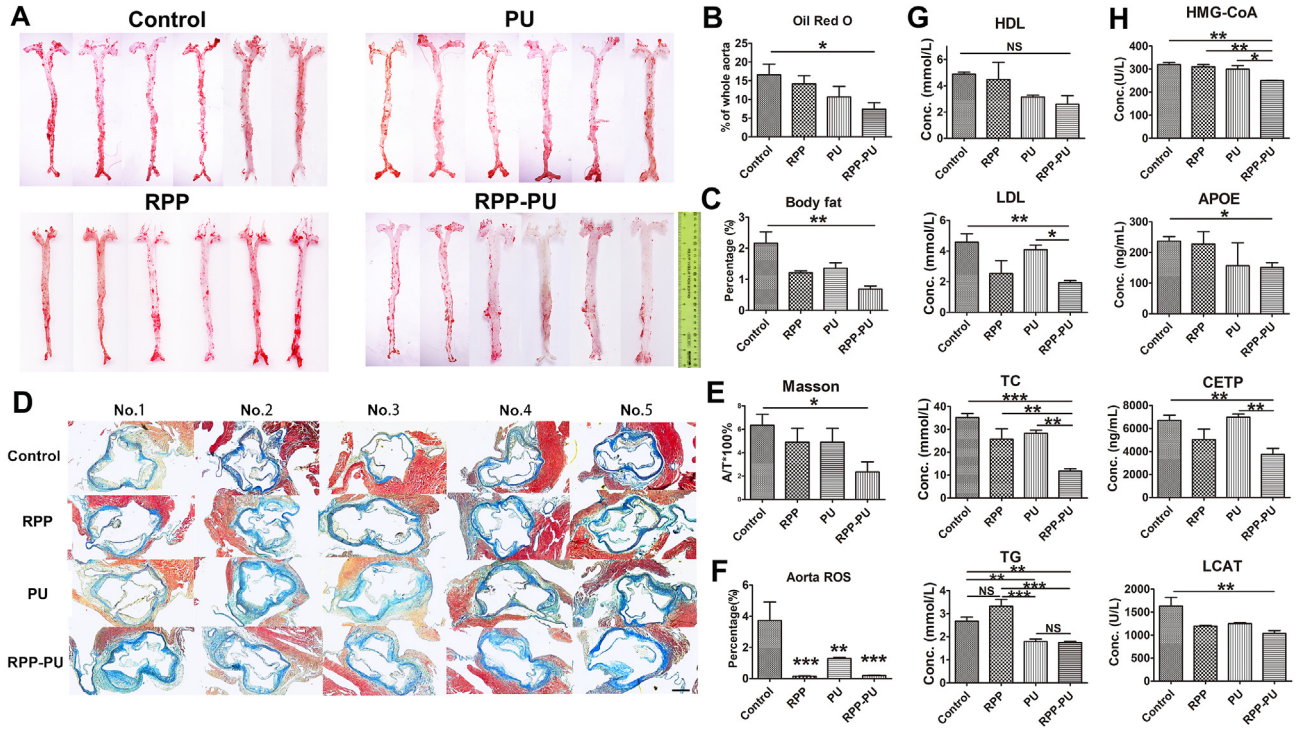

Figure 7 Results from oil red O staining and masson staining as well as the ROS level in the aorta of mice. (A) The wholeaorta was stained with oil red O. Ruler = 10 cm. (B) The oil red O staining fat was quantified. (C) The body fat ratio was calculated. (D, E) Sections from the aortic root of APOE$^{-/-}$ mice were processed by masson staining. Scale bars = 200 μm. (F) Quantitative determination of ROS in the aorta by DCFH-DA. (G) Serum levels of HDL, LDL, TG and TC. (H) Serum levels of HMG-CoA, APOE, CETP, and LCAT. Data are presented as mean ± SD (n = 4−6). *P < 0.05, **P < 0.01, ***P < 0.001. NS, not significant.

3.12. HE and IHC staining of pathological sections of aortic root

HE pathological sections of aortic root were prepared. In Supporting Information Fig. S14, 30 × enlarged figures show the aortic root slides of heart and the shape of the three valves; 100 × enlarged figures show the details of vascular lesions such as foam cells and plaques which were the part indicated by the black arrow. The treatment of atherosclerotic plaque in the RPP-PU group was most effective, and the morphology of blood vessels returned to the level like normal blood vessels (Fig. S14). Almost no obvious foam cells and lipid plaques could be seen in the RPP-PU group.

The IHC staining included MOMA-2 staining of macrophages, SMO staining of SMC, CD3 staining of T cells, and detection of CD68 proteins and MCP-1 in mice aorta (Fig. 8). There was no statistical difference in T cells represented by CD3 (Supporting Information Fig. S15). The Results suggests that it did not cause strong immune responses. The positive distribution of mononuclear macrophages in RPP-PU was slightly increased (Supporting Information Fig. S16). The number of macrophages in vascular walls decreased whereas the number of mononuclear macrophages in the blood increased and the formation of foam cells was inhibited. The numbers of MOMA-2-stained macrophages in the PU group and the RPP-PU group were significantly reduced (Supporting Information Fig. S17) which might decrease the number of foam cells on vascular walls. Plaque formation was decreased and associated with the focal reduction of macrophage infiltration after injury. The number of SMC was significantly reduced in the RPP-PU group (Supporting Information Fig. S18) implying that the proliferation of SMC was inhibited, fibrosis was inhibited and vascular wall thickening was decreased. Compared with the PU group, RPP-PU significantly reduced the MCP-1 level (Supporting Information Fig. S19), decreased the adhesion of monocytes to EC. Overall, RPP-PU could improve various immune and cellular regulations.

4. Discussion

NPs do not change the mechanism of PU itself, mainly through the encapsulation of NPs and the H_2O_2-scavenging of materials to increase the drug effect significantly. About the mechanisms of RPP-PU, we believed that the role of nano delivery vector was better than soluble PU by reducing the oxidative stress, the material could reduce ROS *in vivo* and *in vitro*, and significantly increased the hypolipemic effect of the drug, and also enhanced the antioxidant effect of the drug.

Results from TEM and DLS indicated the favorable dispersibility and expected size of NPs. Some reports have shown that larger particles (at the size of 500−2000 nm) were mostly retained at the injection sites and were picked up by dendritic cells at the injection sites, while smaller particles (at the size of 20−200 nm) were introduced into dendritic cells and macrophages through the process of passive targeting[49]. RPP-PU at about 200 nm in diameter would facilitate drainage to organs.

ROS levels of atherosclerotic disease and other diseases were 10−1000 μmol/L even 10 mmol/L. One of the most important ROS is hydrogen peroxide. All cells produce H_2O_2 from multiple sources. However, on the reason of catalase and peroxidases, the intracellular H_2O_2 is 10 nmol/L or less. From the analysis of

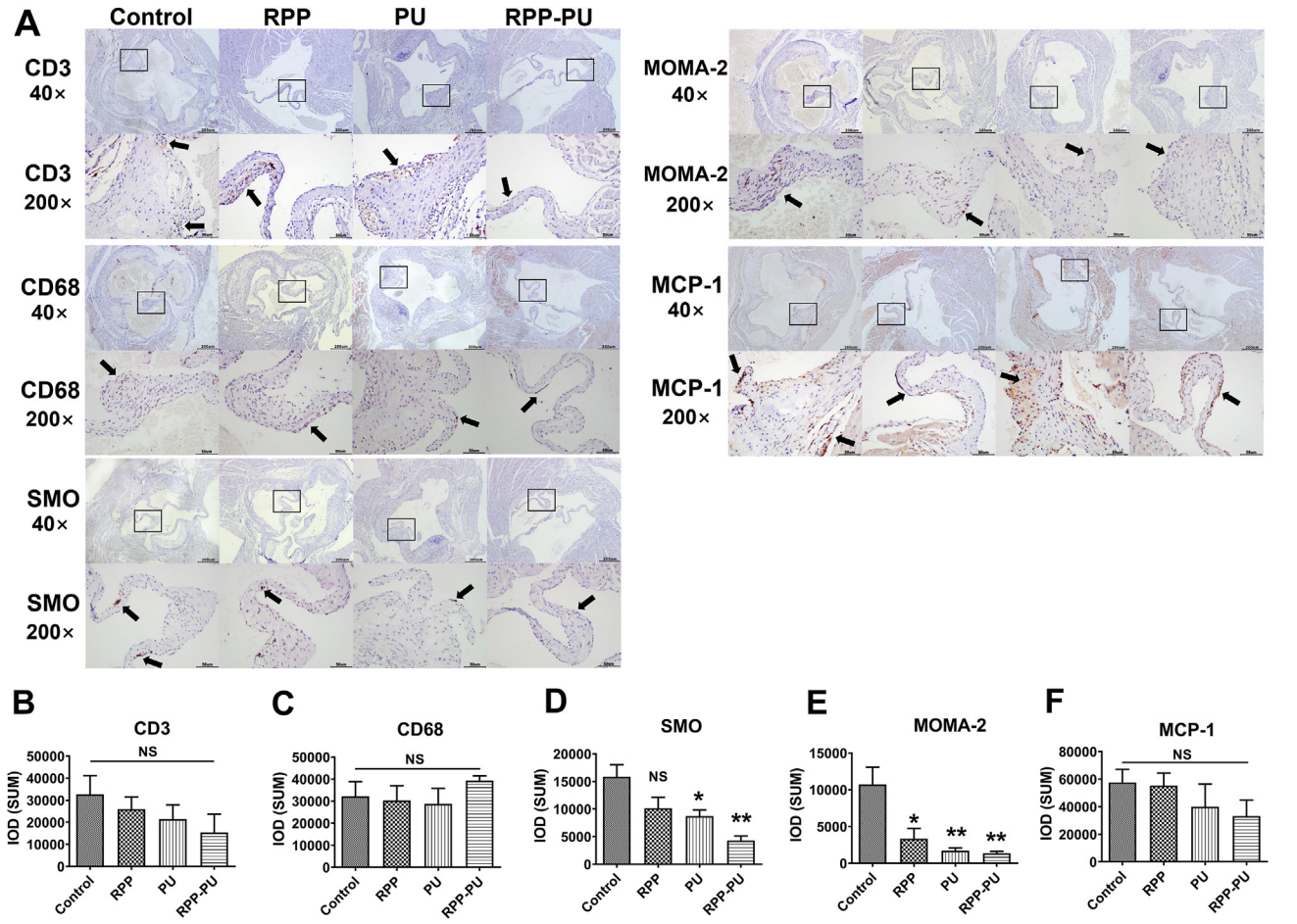

Figure 8 IHC staining of pathological sections from aortic root (CD3, CD68, SMO, MOMA-2, MCP-1). (A) The representative images of IHC 40 × (Scale bars = 200 μm) and images of IHC 200 × (Scale bars = 50 μm). The black arrow points to the antibody positive signal which was brown. (B−F) Content of antibodies was measured by Image J. Data are presented as mean ± SD (n = 4−6). *P < 0.05, **P < 0.01, ***P < 0.001. NS, not significant.

literature and kinetics, the likely normal range for plasma H_2O_2 is 1−5 μmol/L. It goes up as high as 50 μmol/L in inflammatory disease[50,51]. So we chose 10, 100, and 1000 μmol/L H_2O_2 concentration to do the release profile of NPs. A high-fat diet was shown to increase H_2O_2 concentration from 10 to 35 μmol/L[52]. However, in most researches, H_2O_2 response could only reach 100 μmol/L, which cannot meet the needs of treatment for diseases[30]. The H_2O_2-scavenging performance was better from 6s-PLGA-DAr-PO-PEG and the H_2O_2 response sensitivity can be reduced from 40 to 10 μmol/L which was close to the lowest concentration of ROS levels of the pathological environment of atherosclerosis.

The production of ROS and initiation of inflammatory reactions in atherosclerotic lesions are caused by vascular injuries, prolonged exposure to a high level of ROS or inappropriate subcellular localization of ROS may result in detrimental effects[53]. Therefore, we chose H_2O_2-scavenging materials-6s-PLGA-DAr-PO-PEG to remove redundant ROS from the diseased tissues. It is well known that PLGA and PEG have good security. A peroxalate bond was used to connected them and the materials had the H_2O_2-scavenging function. In addition, the addition of diphenyl ring improved the H_2O_2-scavenging sensitivity of polymer. On the other hand, compared with PLGA-PEG over previously reported ones, we use oxalyl chloride to connect PLGA and PEG, which greatly simplifies the synthesis process, makes the experiment easier and yields higher. PEG could increase the long cycle and synergize with RBC, to give full play to the advantages of polymer. In previous studies on ROS-responsive materials, Wang et al.[3] confirmed that a broad-spectrum ROS-eliminating NP could serve as an effective therapy for atherosclerosis. Minami and colleagues[54] demonstrated that APP-103 presented higher sensitivity and specificity to H_2O_2 containing more peroxalate bonds and could reduce tissue injuries and inflammatory responses. The findings also provide evidence of the therapeutic effects delivered by ROS-responsive materials in treating inflammations in atherosclerosis. In brief, considering the increased level of intracellular ROS in local inflammatory processes, the reactivity of NPs to H_2O_2 could facilitate drug release *via* precise targeting and reducing oxidative stress.

Both probucol and the nanomaterials could scavenge the ROS. Their different roles in atherosclerosis treatment were as followed: probucol had antioxidant properties, but the dosage of probucol was too little to remove H_2O_2 from the pathological environment. If the dosage was large, it could produce a sufficient antioxidant effect, but the drug toxicity would also increase. However, the RPP materials had good biocompatibility and degradability. We

used appropriate nanomaterials to remove H_2O_2, and the nanomaterials had highly H_2O_2 removal sensitivity. In addition, nanomaterials had enhanced stability and slow-release behavior which could scavenge the ROS for a long time. In conclusion, the antioxidant effect of drugs was less and transient, and nanomaterials were more sensitive and sustained.

This system achieves the precise targeting of atherosclerosis by the highly sensitive H_2O_2-scavenging nano system. Our experiments also verified that its targeting was derived from the material with H_2O_2 responsiveness. The inherent mechanism for the atherosclerosis targeting might be due to the high-level ROS in atherosclerosis so that nano system with a highly sensitive H_2O_2-scavenging function could release the drug in lesion sites for precise treatment of atherosclerosis. In fact, due to the particle size, nanoparticles are more likely to stay in organs, especially in the liver of metabolic organs, which is inevitable. 30%−99% of nanoparticles will accumulate in the liver after administration into the body. This leads to reduced delivery to the targeted tissue[55]. Moreover, under the long circulation of red blood cells, RP/RPP nanoparticles stayed in organs for a longer time. In blood vessels, compared with other groups, RPP nanoparticles retained significantly more in atherosclerotic vessels, so it still had a strong vascular targeting effect.

The above findings were related to the mechanism of action of PU, in which functions of HMG-CoA, LCAT, CETP, and APOE involved in regulating lipid metabolism were inhibited by PU. The mechanism of lipid-lowering effects of PU mainly resides in lowering LDL and enhancing the reverse transportation of HDL. Compared with the control group and the free PU group, the effects of lowering TG levels in the NPs group were more significant. The overall lipid-lowering effects of NPs were much better than the free PU group. Generally, a moderate increase in HDL level could bring benefits in the treatment of atherosclerosis, while PU could reduce HDL level. Yamamoto et al.[44] explained the beneficial effects of PU on atherosclerosis despite its HDL-lowering effects, suggesting that it could increase reverse cholesterol transportation at the same time. In fact, PU could change the structures and functions of HDL subtypes, facilitating the transportation of cholesterol from peripheral tissues, including transportation from pathological arterial walls to the liver. Advanced atherosclerotic lesions are also further weakened by the pronounced local activity of matrix-degrading proteases as well as immature neo vessels sprouting into the lesion[56]. And RPP-PU NPs had a good trend effect of inhibition of protease activity, and dampened inflammatory cell recruitment.

Compared with bare PU, RPP-PU could improve the phagocytosis of macrophages, relieve endothelial dysfunctions, reduce the intracellular levels of lipids, restrain the levels of inflammatory factors as well. Recent studies have demonstrated that atherosclerotic plaques were determined by pathological changes on vascular walls rather than the severity of stenosis. Rupture of the fibrous cap of an inflamed atherosclerotic plaque is considered the most common trigger of thrombosis and ischemia[57]. Hence, inhibiting inflammation is critical in inhibiting the development of atherosclerosis.

The recruitment of monocytes to vascular walls was a crucial step in the process of macrophage accumulation in atherosclerotic plaques[58]. Reduction on MCP-1 level indicated decreased recruitment of monocytes to vascular walls and contributed to reduced foam cell formations, thus inhibiting the progression of inflammations. It demonstrated that the risk of cardiovascular events in patients with atherosclerosis could be reduced by reducing inflammations induced by high-level ROS and by adjustments of blood cholesterol levels, highlighting the potential of this anti-oxidative and anti-inflammatory treatment in improving clinical outcomes.

5. Conclusions

In summary, to improve the effects of treatment for atherosclerosis, we designed a highly sensitive H_2O_2-scavenging nano-bionic system to selectively release PU in pathological microenvironments. Our study demonstrate that RPP-PU were satisfactory in terms of stability, H_2O_2-eliminating effects *in vitro*, cell compatibility, and safety *in vivo*. The RPP-PU group presented significantly decreased body fat rate and low serum level of LDL, decreased area of vascular plaques, and formations of fibers and collagen in the atherosclerotic lesions. This H_2O_2-scavenging nano-bionic system can provide a new treatment option for atherosclerosis. It exploits multiple advantages of lowering lipid levels, prolonging circulation time, anti-oxidative and anti-inflammatory potentials.

Acknowledgments

This work was supported by grants from the National Natural Science Funds of China (31771097, 82072080, 82070301) and CAMS Innovation Fund for Medical Sciences (CIFMS, 2021-I2M-1-058, China). This project was also supported by Special Program for High-Tech Leader & Team of Tianjin Government and Tianjin Innovation Promotion Plan Key Innovation Team of Immunoreactive Biomaterials.

Author contributions

Xiaoyu Liang completed the experimental design, did a lot of experiments, data processing and analysis, wrote and revised manuscript. Huiyang Li did a lot of animal experiments, completed data processing and analysis of relative data and revised manuscript. Xuanling Li contributed to the design of material experiments and provided materials. Xinxin Tian and Aiai Zhang conducted some animal experiments. Qingzhi Luo developed hematological testing techniques and contributed to several blood tests. Jianwei Duan and Youlu Chen performed some cell experiments. Liyun Pang contributed to laser confocal experiments. Chen Li guided manuscript writing. Xing-jie Liang contributed to the experimental design and promoted the development of the whole project. Jing Yang and Yong Zeng contributed to the development of the experimental design, revised the manuscript, and supervised the process of the whole project. All of the authors have read and approved the final manuscript.

Conflicts of interest

The authors have no conflicts of interest to declare.

Appendix A. Supporting information

Supporting data to this article can be found online at https://doi.org/10.1016/j.apsb.2022.04.002.

References

1. Back M, Yurdagul AJ, Tabas I, Oorni K, Kovanen PT. Inflammation and its resolution in atherosclerosis: mediators and therapeutic opportunities. *Nat Rev Cardiol* 2019;**16**:389−406.
2. Peter L. Mechanisms of acute coronary syndromes and their implications for therapy. *N Engl J Med* 2013;**368**:2004−13.
3. Wang YQ, Li LL, Zhao WB, Dou Y, An HJ, Tao H, et al. Targeted therapy of atherosclerosis by a broad-spectrum reactive oxygen species scavenging nanoparticle with intrinsic anti-inflammatory activity. *ACS Nano* 2018;**12**:8943−60.
4. Wang XL, Li XL, Liang XY, Liang JY, Zhang C, Yang J, et al. ROS-responsive capsules engineered from green tea polyphenol-metal networks for anticancer drug delivery. *J Mater Chem B* 2018;**6**:1000−10.
5. Förstermann U, Xia N, Li HG. Roles of vascular oxidative stress and nitric oxide in the pathogenesis of atherosclerosis. *Circ Res* 2017;**120**: 713−35.
6. Zhu XW, Xie HZ, Liang XY, Li XL, Duan JW, Chen YX, et al. Bilayered nanoparticles with sequential release of VEGF gene and paclitaxel for restenosis inhibition in atherosclerosis. *ACS Appl Mater Interfaces* 2017;**9**:27522−32.
7. Kattoor AJ, Pothineni NVK, Palagiri D, Mehta JL. Oxidative stress in atherosclerosis. *Curr Atheroscler Rep* 2017;**19**:42.
8. Tejero J, Shiva S, Gladwin MT. Sources of vascular nitric oxide and reactive oxygen species and their regulation. *Physiol Rev* 2019;**99**: 311−79.
9. Sies H. Hydrogen peroxide as a central redox signaling molecule in physiological oxidative stress: oxidative eustress. *Redox Biol* 2017;**11**: 613−9.
10. Li J, Yang Y, Zhao MH, Xu H, Ma JY, Wang SN. Improved oral bioavailability of probucol by dry media-milling. *Mater Sci Eng C Mater Biol Appl* 2017;**78**:780−6.
11. Guo XK, Wang L, Xia XS, Wang PL, Li X. Effects of atorvastatin and/or probucol on recovery of atherosclerosis in high-fat-diet-fed apolipoprotein E-deficient mice. *Biomed Pharmacother* 2019;**109**: 1445−53.
12. Yamashita S, Masuda D, Matsuzawa Y. Did we abandon probucol too soon? *Curr Opin Lipidol* 2015;**26**:304−16.
13. Han L, Yang Q, Shen T, Qing J, Wang J. Lymphatic transport of orally administered probucol-loaded mPEG-DSPE micelles. *Drug Deliv* 2015;**23**:1−7.
14. Li GP, Yin L, Liu T, Zhang XT, Xu G, Xu YM, et al. Role of probucol in preventing contrast-induced acute kidney injury after coronary interventional procedure. *Am J Cardiol* 2009;**103**:512−4.
15. Qi R, Li YZ, Chen C, Cao YN, Yu MM, Xu L, et al. G5-PEG PAMAM dendrimer incorporating nanostructured lipid carriers enhance oral bioavailability and plasma lipid-lowering effect of probucol. *J Contr Release* 2015;**210**:160−8.
16. Lin ZA, Xiao Y, Wang L, Yin YQ, Zheng JN, Yang HH, et al. Facile synthesis of enzyme-inorganic hybrid nanoflowers and their application as an immobilized trypsin reactor for highly efficient protein digestion. *RSC Adv* 2014;**4**:13888−91.
17. Kanthi Y, de la Zerda A, Smith BR. Nanotherapeutic shots through the heart of plaque. *ACS Nano* 2020;**14**:1236−42.
18. Dou Y, Chen Y, Zhang XJ, Xu XQ, Chen YD, Guo JW, et al. Non-proinflammatory and responsive nanoplatforms for targeted treatment of atherosclerosis. *Biomaterials* 2017;**143**:93−108.
19. Lobatto ME, Calcagno C, Millon A, Senders ML, Fay F, Robson PM, et al. Atherosclerotic plaque targeting mechanism of long-circulating nanoparticles established by multimodal imaging. *ACS Nano* 2015;**9**:1837−47.
20. Katsuki S, Matoba T, Nakashiro S, Sato K, Koga J, Nakano K, et al. Nanoparticle-mediated delivery of pitavastatin inhibits atherosclerotic plaque destabilization/rupture in mice by regulating the recruitment of inflammatory monocytes. *Circulation* 2014;**129**:896−906.
21. Mitragotri S, Lahann J. Materials for drug delivery: innovative solutions to address complex biological hurdles. *Adv Mater* 2012;**24**: 3717−23.
22. Brenner JS, Pan DC, Myerson JW, Marcos-Contreras OA, Villa CH, Patel P, et al. Red blood cell-hitchhiking boosts delivery of nanocarriers to chosen organs by orders of magnitude. *Nat Commun* 2018; **9**:2684.
23. Kroll AV, Fang RH, Zhang LF. Biointerfacing and applications of cell membrane-coated nanoparticles. *Bioconjugate Chem* 2017;**28**:23−32.
24. Dehaini D, Wei XL, Fang RH, Masson S, Angsantikul P, Luk BT, et al. Erythrocyte-platelet hybrid membrane coating for enhanced nanoparticle functionalization. *Adv Mater* 2017;**29**:1606209.
25. Zhang L, Wang ZZ, Zhang Y, Cao FF, Dong K, Ren JS, et al. Erythrocyte membrane cloaked metal-organic framework nanoparticle as biomimetic nanoreactor for starvation-activated colon cancer therapy. *ACS Nano* 2018;**12**:10201−11.
26. Guo YY, Wang D, Song QL, Wu TT, Zhuang XT, Bao YL, et al. Erythrocyte membrane-enveloped polymeric nanoparticles as nanovaccine for induction of antitumor immunity against melanoma. *ACS Nano* 2015;**9**:6918−33.
27. Zhang Y, Zhang JH, Chen WS, Angsantikul P, Spiekermann KA, Fang RH, et al. Erythrocyte membrane-coated nanogel for combinatorial antivirulence and responsive antimicrobial delivery against Staphylococcus aureus infection. *J Contr Release* 2017;**263**: 185−91.
28. Zhao ZM, Ukidve A, Gao YS, Kim J, Mitragotri S. Erythrocyte leveraged chemotherapy (ELeCt): nanoparticle assembly on erythrocyte surface to combat lung metastasis. *Sci Adv* 2019;**5**:eaax9250.
29. Yang BW, Chen Y, Shi JL. Reactive oxygen species (ROS)-based nanomedicine. *Chem Rev* 2019;**119**:4881−985.
30. Saravanakumar G, Kim J, Kim WJ. Reactive-oxygen-species-responsive drug delivery systems: promises and challenges. *Adv Sci* 2017;**4**: 1600124.
31. Liang XY, Duan JW, Li XL, Zhu XW, Chen YL, Wang XL, et al. Improved vaccine-induced immune responses *via* a ROS-triggered nanoparticle-based antigen delivery system. *Nanoscale* 2018;**10**: 9489−503.
32. Liu C, Zhu XW, Wang XL, Miao DD, Liang XY, Wang CW, et al. Hydrogen peroxide-responsive micelles self-assembled from a peroxalate ester-containing triblock copolymer. *Biomater Sci* 2016;**4**: 255−7.
33. Duan JW, Liu C, Liang XY, Li XL, Chen YL, Chen ZG, et al. Protein delivery nanosystem of six-arm copolymer poly(epsilon-caprolactone)-poly(ethylene glycol) for long-term sustained release. *Int J Nanomed* 2018;**13**:2743−54.
34. Zhu XW, Liu C, Duan JW, Liang XY, Li XL, Sun HF, et al. Synthesis of three-arm block copolymer poly(lactic-*co*-glycolic acid)-poly(ethylene glycol) with oxalyl chloride and its application in hydrophobic drug delivery. *Int J Nanomed* 2016;**11**:6065−77.
35. Hu CMJ, Zhang L, Aryal S, Cheung C, Fang RH, Zhang LF. Erythrocyte membrane-camouflaged polymeric nanoparticles as a biomimetic delivery platform. *Proc Natl Acad Sci U S A* 2011;**108**: 10980−5.
36. Liang XY, Li XL, Duan JW, Chen YL, Wang XL, Pang LY, et al. Nanoparticles with CD44 targeting and ROS triggering properties as effective *in vivo* antigen delivery system. *Mol Pharm* 2018;**15**:508−18.
37. Yang J, Sun HF, Song CX. Preparation, characterization and *in vivo* evaluation of pH-sensitive oral insulin-loaded poly(lactic-*co*-glycolicacid) nanoparticles. *Diabetes Obes Metabol* 2012;**14**: 358−64.
38. Yang J, Zeng Y, Zhang C, Chen YX, Yang ZY, Li YJ, et al. The prevention of restenosis *in vivo* with a *VEGF* gene and paclitaxel co-eluting stent. *Biomaterials* 2013;**34**:1635−43.
39. Zhang WB, Yang F, Wang Y, Jiao FZ, Zhang HY, Wang LW, et al. Inhibition of HDAC6 attenuates LPS-induced inflammation in macrophages by regulating oxidative stress and suppressing the TLR4-MAPK/NF-κB pathways. *Biomed Pharmacother* 2019;**117**: 109166.
40. Nemmar A, Beegam S, Yuvaraju P, Yasin J, Tariq S, Attoub S, et al. Ultrasmall superparamagnetic iron oxide nanoparticles acutely

promote thrombosis and cardiac oxidative stress and DNA damage in mice. *Part Fibre Toxicol* 2016;**13**:22.
41. Mohammadpour R, Yazdimamaghani M, Cheney DL, Jedrzkiewicz J, Ghandehari H. Subchronic toxicity of silica nanoparticles as a function of size and porosity. *J Contr Release* 2019;**304**:216−32.
42. Miller CP, Hammond CW, Anderle SK. Studies on susceptibility to infection following ionizing radiation. V. Comparison of intraperitoneal and intravenous challenge at intervals following different doses of X-radiation. *J Exp Med* 1960;**111**:773−84.
43. Fedrigo M, Feltrin G, Poli F, Frigo AC, Benazzi E, Gambino A, et al. Intravascular macrophages in cardiac allograft biopsies for diagnosis of early and late antibody-mediated rejection. *J Heart Lung Transplant* 2013;**32**:404−9.
44. Yamamoto S, Tanigawa H, Li XY, Komaru Y, Billheimer JT, Rader DJ. Pharmacologic suppression of hepatic ATP-binding cassette transporter 1 activity in mice reduces high-density lipoprotein cholesterol levels but promotes reverse cholesterol transport. *Circulation* 2011;**124**:1382−90.
45. Kim JH, Hong KW, Bae SS, Shin YI, Choi BT, Shin HK. Probucol plus cilostazol attenuate hypercholesterolemia-induced exacerbation in ischemic brain injury *via* anti-inflammatory effects. *Int J Mol Med* 2014;**34**:687−94.
46. Daugherty A, Zweifel BS, Schonfeld G. The effects of probucol on the progression of atherosclerosis in mature Watanabe heritable hyperlipidaemic rabbits. *Br J Pharmacol* 1991;**103**:1013−8.
47. Wang Y, Zhang K, Qin X, Li TH, Qiu JH, Yin TY, et al. Biomimetic nanotherapies: red blood cell based core−shell structured nanocomplexes for atherosclerosis management. *Adv Sci (Weinh)* 2019;**6**:1900172.
48. Maruf A, Wang Y, Luo L, Zhong Y, Nurhidayah D, Liu B, et al. Nanoerythrocyte membrane-enveloped ROS-responsive 5-aminolevulinic acid prodrug nanostructures with robust atheroprotection. *Part Part Syst Char* 2020;**37**:2000021.
49. Shi GN, Zhang CN, Xu R, Niu JF, Song HJ, Zhang XY, et al. Enhanced antitumor immunity by targeting dendritic cells with tumor cell lysate-loaded chitosan nanoparticles vaccine. *Biomaterials* 2017;**113**:191−202.
50. Forman HJ, Bernardo A, Davies KJ. What is the concentration of hydrogen peroxide in blood and plasma?. *Arch Biochem Biophys* 2016;**603**:48−53.
51. Pelicano H, Carney D, Huang P. ROS stress in cancer cells and therapeutic implications. *Drug Resist Updates* 2004;**7**:97−110.
52. Roberts CK, Barnard RJ, Sindhu RK, Jurczak M, Ehdaie A, Vaziri ND. A high-fat, refined-carbohydrate diet induces endothelial dysfunction and oxidant/antioxidant imbalance and depresses NOS protein expression. *J Appl Physiol* 2005;**98**:203−10 (1985).
53. Niemann B, Rohrbach S, Miller MR, Newby DE, Fuster V, Kovacic JC. Oxidative stress and cardiovascular risk: obesity, diabetes, smoking, and pollution: Part 3 of a 3-Part series. *J Am Coll Cardiol* 2017;**70**:230−51.
54. Minami K, Bae S, Uehara H, Zhao C, Lee DW, Iske J, et al. Targeting of intragraft reactive oxygen species by APP-103, a novel polymer product, mitigates ischemia/reperfusion injury and promotes the survival of renal transplants. *Am J Transplant* 2020;**20**:1527−37.
55. Zhang YN, Poon W, Tavares AJ, McGilvray ID, Chan WCW. Nanoparticle-liver interactions: cellular uptake and hepatobiliary elimination. *J Contr Release* 2016;**240**:332−48.
56. Silvestre-Roig C, de Winther MP, Weber C, Daemen MJ, Lutgens E, Soehnlein O. Atherosclerotic plaque destabilization: mechanisms, models, and therapeutic strategies. *Circ Res* 2014;**114**:214−26.
57. Savastano LE, Zhou Q, Smith A, Vega K, Murga-Zamalloa C, Gordon D, et al. Multimodal laser-based angioscopy for structural, chemical and biological imaging of atherosclerosis. *Nat Biomed Eng* 2017;**1**:0023.
58. Swirski FK, Nahrendorf M. Leukocyte behavior in atherosclerosis, myocardial infarction, and heart failure. *Science* 2013;**339**:161−6.